

Galaxy cluster matter profiles: I. Self-similarity and mass calibration

A. Singh^{1,2,*}, J. J. Mohr^{1,2}, C. T. Davies¹, S. Bocquet¹, S. Grandis^{1,3}, M. Klein¹, J. L. Marshall³²,
M. Aguena⁴, S. S. Allam⁵, O. Alves⁶, F. Andrade-Oliveira^{4,7}, D. Bacon⁸, S. Bhargava⁹, D. Brooks¹⁰,
A. Carnero Rosell^{11,4}, J. Carretero¹², M. Costanzi^{13,14,15}, L. N. da Costa⁴, M. E. S. Pereira¹⁶, S. Desai¹⁷, H. T. Diehl⁵,
P. Doel¹⁰, S. Everett¹⁸, B. Flaugher⁵, J. Frieman^{5,19}, J. García-Bellido²⁰, E. Gaztanaga^{21,8,22}, R. A. Gruendl^{23,24},
G. Gutierrez⁵, D. L. Hollowood²⁵, K. Honscheid^{26,27}, D. J. James²⁸, K. Kuehn^{29,30}, M. Lima^{31,4}, J.
Mena-Fernández³³, F. Menanteau^{23,24}, R. Miquel^{34,12}, J. Myles³⁵, A. Pieres^{4,36}, A. K. Romer⁹, S. Samuroff³⁷,
E. Sanchez³⁸, D. Sanchez Cid³⁸, I. Sevilla-Noarbe³⁸, M. Smith³⁹, E. Suchyta⁴⁰, M. E. C. Swanson²³, G. Tarle⁶, C. To²⁶,
D. L. Tucker⁵, V. Vikram⁴¹, N. Weaverdyck^{42,43}, and P. Wiseman³⁹
(the DES and SPT Collaborations)

Affiliations at the end of the paper

Received—; accepted—

ABSTRACT

We present a study of the weak lensing matter profiles of 698 South Pole Telescope (SPT) thermal Sunyaev-Zel'dovich effect (tSZE) selected galaxy clusters in the redshift range $0.25 < z < 0.94$ that have associated weak gravitational lensing shear profiles from the Dark Energy Survey (DES). When rescaled to account for the mass dependent size and the redshift dependent density, this SPT cluster sample when averaged within bins of redshift and tSZE detection significance shows a lower dispersion in the matter profiles than the unscaled versions. Galaxy clusters from hydrodynamical simulations also exhibit matter profiles that suggest a high degree of self-similarity, with RMS variation among the rescaled average matter profiles improving by a factor of ≈ 6 with redshift and ≈ 23 with mass in comparison to the unscaled average matter profiles. We employ this regularity in a new Bayesian method for weak lensing mass calibration, simultaneously constraining richness-mass and tSZE detection significance-mass relations using average, rescaled cluster matter profiles. We validate the method using realistic mock datasets and present scaling relation constraints for the SPT×DES sample, where we constrain the amplitude, mass trend, redshift trend, and intrinsic scatter. Our scaling relation results are in agreement with the mass calibration derived from the recent cosmological analysis of the SPT×DES data based on a cluster-by-cluster lensing calibration. Our new mass calibration technique offers higher efficiency when compared to the single cluster calibration technique. In addition, the average rescaled matter profiles offer high signal-to-noise constraints on the shape of real cluster profiles which is in good agreement with the Λ CDM model. In the future it will provide improved insights into baryon feedback, the collisional nature of dark matter and modified gravity models.

Key words. galaxies: clusters: general – gravitational lensing: weak – cosmology: large-scale structure of Universe

1. Introduction

Galaxy clusters constitute the most massive collapsed halos in the Universe. Studying their abundance as a function of redshift and mass provides insights into structure formation history and therefore serves as a powerful tool for constraining cosmological models (e.g., White et al. 1993; Haiman et al. 2001; Vikhlinin et al. 2009; Mantz et al. 2010; Planck Collaboration & et al. 2016; Chiu et al. 2023; Bocquet et al. 2024). The ability to measure cluster masses accurately plays an important role in cluster cosmological studies, enabling constraints on the rate of cosmic structure growth, the dark energy equation of state, and other cosmological parameters such as the amplitude of matter fluctuations and the matter density parameter. The development of robust weak lensing and CMB lensing informed mass calibration techniques (Becker & Kravtsov 2011; von der Linden et al. 2014; Dietrich et al. 2018; Zubeldia & Challinor 2019; Grandis et al. 2021; Bocquet et al. 2023) and the availability of associated high quality weak lensing (WL) datasets from, e.g., Hyper Suprime-Cam Subaru Strategic Program (HSC-SSP), Dark

Energy Survey (DES) and Kilo-Degree Survey (KiDS) has set the stage for progress in constraining the standard Λ CDM and w CDM parameters (Costanzi et al. 2019; Abbott et al. 2020; Costanzi et al. 2021; To et al. 2021; Chiu et al. 2023; Bocquet et al. 2024; Ghirardini et al. 2024) as well as model extensions including modification of general relativity and interacting dark matter (e.g., Mantz et al. 2014; Cataneo et al. 2015; Mazoun et al. 2023; Vogt et al. 2024).

These same WL datasets can be employed to study the matter distribution within galaxy clusters. A challenge is that in the existing WL datasets based on large photometric surveys, the matter profiles of individual clusters often have low signal-to-noise ratio (SNR). Combining WL matter profiles from multiple galaxy clusters provides a way to improve the SNR and also to reduce the intrinsic variations in the matter distribution from cluster to cluster that arise from their different formation histories. Previous works have employed WL measurements of multiple clusters to constrain cluster masses by combining tangential shear profiles or projected matter profiles of clusters (Oguri & Takada 2011; Umetsu et al. 2016; McClintock et al. 2018; Bellagamba et al. 2019; Giocoli et al. 2021; Lesci et al. 2022). A challenge

* aditya.singh@physik.lmu.de

in this approach is that there are systematic variations in the projected matter profiles of galaxy clusters with cluster mass and redshift. An average WL matter profile therefore reflects the characteristics of the cluster sample, and it depends sensitively on the distribution of the sample in mass and redshift. Tangential shear profiles are sensitive not only to the cluster characteristics but also to the redshift distribution of the WL source galaxies.

If the systematic variations of the matter profiles with mass and redshift can be accurately characterized, then they can also be scaled out, enabling average matter profiles of high SNR that are largely independent of the characteristics of the cluster sample from which they are constructed. In particular, if cluster matter distributions are approximately self-similar in nature— that is, they exhibit similar shapes that vary systematically with mass and redshift— then these systematic trends can be easily removed. Approximate self-similarity is a generic prediction of gravitational structure formation (Kaiser 1986). In N-body simulations, cluster halos are well described by so-called Navarro-Frank-White (NFW) models (Navarro et al. 1997) that exhibit weak trends in concentration or shape with mass and redshift. In hydrodynamical simulation, self-similar behavior has been seen in cluster gas profiles (Lau et al. 2015) and pressure profiles (Nelson et al. 2014). Observationally, approximate self-similarity has been demonstrated in intracluster medium (ICM) density, pressure profiles and temperature profiles (Vikhlinin et al. 2006; Arnaud et al. 2010; Baldi et al. 2012; McDonald et al. 2014), whereas WL studies of cluster matter profiles have tended to focus on whether NFW is a good description (e.g., Umetsu et al. 2014).

In this analysis we use hydrodynamic structure formation simulations and direct WL observations of cluster samples to examine cluster matter profiles, revealing remarkable consistency and approximate self-similarity of simulated and real matter profiles. We then exploit this self-similarity to study high SNR cluster matter profiles and to employ them to perform mass calibration of mass-observable relations. This mass calibration approach offers a computationally more efficient technique to analyze large cluster WL datasets compared to a cluster-by-cluster approach (Bocquet et al. 2019; Bocquet et al. 2023), without loss of information.

The paper is organized as follows. We present the simulated and observed dataset in Section 2. The self-similarity of galaxy cluster matter profiles is explored in Section 3. The mass calibration method along with the likelihood calculation and the hydro-dynamical model is discussed in Section 4. In Section 5 we validate the analysis method using mock data and present the results using the SPT clusters and DES-WL data. We conclude with a summary and outlook in Section 6.

Throughout the paper we employ a flat Λ CDM cosmology with parameters $\Omega_m = 0.3$, and $h = 0.7$. All uncertainties are quoted at the 68 percent credibility level, unless otherwise specified.

2. Data

In this section, we first describe the data used in our work: the SPT cluster catalog, and Dark Energy Survey (Y3) weak-lensing and photometric redshift measurements. Then we summarize the simulation datasets from *Magneticum* and *Illustris-TNG*, which are used to explore the impact of baryons.

2.1. SPT Cluster Catalogs

We use a combination of two thermal Sunyaev-Zel'dovich effect (tSZE) selected cluster catalogs that have been extracted from

surveys carried out by the South Pole Telescope (Carlstrom et al. 2011) collaboration: SPT-SZ (Bleem et al. 2015; Klein et al. 2023) and SPTpol-500d (Bleem et al. 2023). The SPT-SZ survey covers $2,500 \text{ deg}^2$ in the southern sky, while the SPTpol-500d survey pushes to a greater depth within a 500 deg^2 patch inside the SPT-SZ survey. Galaxy cluster candidates are selected from the mm-wave maps at 90 and 150 GHz using a matched filter technique (Melin et al. 2006), which employs galaxy cluster tSZE models with a range of angular scales (Vanderlinde et al. 2010). Only cluster candidates at redshifts $z > 0.25$ are considered, because objects at lower redshifts are more strongly impacted by the matched filtering, which is designed to remove atmospheric noise as well as increased noise contributions from the primary CMB. At low redshift the angular scales filtered out overlap with the scales important for the galaxy cluster tSZE, strongly impacting the candidate detection significance and thereby complicating its use as a cluster halo mass proxy.

These cluster candidates are then studied using the Multi-Component Matched Filter cluster confirmation tool (MCMF; Klein et al. 2018). This processing results in a cluster catalog that includes measurements of optical richnesses $\hat{\lambda}$, sky positions and redshifts. The measured optical richness allows for efficient removal of contaminants from the tSZE candidate list by evaluating the likelihood of being random superposition of unassociated optical systems with tSZE noise fluctuations (Klein et al. 2023; Bleem et al. 2023). The exclusion threshold corresponds to an observed richness threshold that varies with redshift $\hat{\lambda}_{\min}(z)$ (Klein et al. 2019) and has been determined by analyzing the richness distributions along random lines of sight within the survey. The final cluster catalogs have constant contamination fraction at all redshifts.

The selection threshold in the tSZE detection significance ($\hat{\zeta}$) is $\hat{\zeta} > 4.25$ for SPTpol-500d and $\hat{\zeta} > 4.5$ for SPT-SZ, while the MCMF selection threshold $\hat{\lambda}_{\min}(z)$ is adjusted to maintain a contamination fraction of $< 2\%$ in the final MCMF-confirmed cluster lists from both surveys.

2.2. DES-Y3 lensing

The Dark Energy Survey is a photometric survey in five broadband filters (*grizY*) which covers an area of $\sim 5,000 \text{ deg}^2$ in the southern sky. The survey was conducted using the Dark Energy Camera (DECam; Flaugher et al. 2015) at the 4m Blanco telescope at the Cerro Tololo Inter-American Observatory (CTIO) in Chile. In this work, we use weak lensing data from the first three years of observations (DES Y3), which cover the entire $5,000 \text{ deg}^2$ survey footprint.

The DES Y3 shape catalog (Gatti & Sheldon et al. 2021) is constructed from the *r, i, z*-bands using the METACALIBRATION pipeline (Huff & Mandelbaum 2017; Sheldon & Huff 2017). Other DES Y3 works contain detailed information on the Point-Spread Function modeling (Jarvis et al. 2021), the photometric dataset (Sevilla-Noarbe et al. 2021), and image simulations (MacCrann et al. 2022). After all source selection cuts, the shear catalog consists of roughly 100 million galaxies over an area of $4,143 \text{ deg}^2$. The typical source density is 5 to 6 arcmin^{-2} , depending on the exact choices of a specific analysis.

Our work follows the selection of lensing source galaxies in four tomographic bins as employed in the DES 3x2pt analysis (Abbott et al. 2022). The selection is defined and calibrated in Myles et al. (2021); Gatti et al. (2022). In which, source redshifts are estimated using Self-Organizing Maps Photo-z (SOMPZ). The final calibration accounts for the (potentially correlated) systematic uncertainties in source redshifts and shear measurements.

For each tomographic source bin, the mean redshift distribution is provided, and the systematic uncertainties are captured using 1,000 realizations of the source redshift distribution. The amplitude of source redshift distribution is scaled by factor $1 + m$ to account for the multiplicative shear bias m . In addition to the tomographic bins and SOMPZ, we use Directional Neighbourhood Fitting (DNF; De Vicente et al. 2016) galaxy photo-z estimates when determining the expected fraction of the lensing source galaxy population in each tomographic bin that is contributed by member galaxies from a particular cluster of interest– the so-called cluster member contamination.

2.3. Hydrodynamical Simulations

In this work, we use the *Magneticum* Pathfinder suite of cosmological hydrodynamical simulations (Hirschmann et al. 2014; Teklu et al. 2015; Beck et al. 2016; Bocquet et al. 2016; Dolag et al. 2017). We use Box1, which has a box size of $896 h^{-1} \text{Mpc}$ on a side with 2×1526^3 particles and the particle mass $1.3 \times 10^{10} h^{-1} M_{\odot}$ for dark matter particles, and $2.6 \times 10^9 h^{-1} M_{\odot}$ for gas particles. The simulation is run with cosmological parameters ($\Omega_m = 0.272$, $\Omega_b = 0.0457$, $H_0 = 70.4$, $n_s = 0.963$, $\sigma_8 = 0.809$), which correspond to the WMAP7 constraints for a spatially flat ΛCDM model (Komatsu et al. 2011). From this simulation, we use snapshots at five redshifts $z_{\text{snap}} = 0.01, 0.25, 0.47, 0.78, 0.96$.

In addition, we also use the data from Illustris-TNG300-1 (Pillepich et al. 2018; Marinacci et al. 2018; Springel et al. 2018; Nelson et al. 2018; Naiman et al. 2018; Nelson et al. 2019). These include 2×2500^3 resolution elements for a box size of $205 h^{-1} \text{Mpc}$ on a side. The cosmology corresponds to the Planck2015 constraints for a spatially flat ΛCDM cosmology (Planck Collaboration & et al. 2016): $\Omega_m = 0.3089$, $\Omega_b = 0.0486$, $\sigma_8 = 0.8159$, $n_s = 0.9667$, and $h = 0.6774$. We use snapshots corresponding to redshift $z_{\text{snap}} = 0.01, 0.24, 0.42, 0.64, 0.95$.

From these simulation snapshots, we then extract halos with $M_{200c} > 3 \times 10^{13} h^{-1} M_{\odot}$. Shear maps are generated following Grandis et al. (2021) in a cylinder with a projection depth of $20 h^{-1} \text{Mpc}$.

3. Self-similarity in Cluster Matter Profiles

Gravitational lensing is the phenomenon through which photon geodesics are perturbed by gravitational potentials. For a distant galaxy, this results in a distortion of the observed image of a galaxy relative to its true shape (Schneider 2006). In this work, we are interested in WL, where distortions in source galaxy images induced by intervening matter along the line of sight are small. In this regime, the WL signal must be extracted through statistical correlations of source galaxies. The observable of interest in this context is the reduced shear, which is defined as

$$g = \frac{\gamma}{1 - \kappa}, \quad (1)$$

where γ is the weak lensing shear and κ is the weak lensing convergence (for detailed explanation see Schneider (2006)). In the weak lensing regime where $\kappa \ll 1$, we can approximate $g \approx \gamma$. The ensemble averaged source ellipticity, e , and the shear response, R_{γ} is related to the reduced shear as

$$\langle g \rangle = \langle R_{\gamma} \rangle^{-1} \langle e \rangle. \quad (2)$$

R_{γ} is the average response of the measured ellipticity to a shear. Due to instrumental effects and noise this shear response typically

is less than 1. The tangential reduced shear profile induced by an object with a projected mass distribution $\Sigma(R)$ is related to the critical surface mass density Σ_{crit} by

$$\Delta\Sigma(R) = \Sigma_{\text{crit}} \gamma_t(R) = \langle \Sigma(< R) \rangle - \Sigma(R), \quad (3)$$

where Σ_{crit} depends on the geometry of the source-lens system and is defined as

$$\Sigma_{\text{crit}}(z_s, z_l) = \frac{c^2}{4\pi G} \frac{D_s}{D_l D_{ls}}, \quad (4)$$

where z_s and z_l are the source and lens redshifts, respectively, and D_s, D_l, D_{ls} are the angular diameter distances to the source, lens, and between the source-lens pair. For a given source redshift distribution $P(z_s)$, we can compute the average lensing efficiency for a given lens as

$$\Sigma_{\text{crit}}^{-1}(z_l) = \int dz_s P(z_s) \Sigma_{\text{crit}}^{-1}(z_s, z_l). \quad (5)$$

When $z_s \leq z_l$, $\Sigma_{\text{crit}}^{-1}$ is defined to be zero. From Eq. 3 we can see that the differential surface mass density at a given projected radius R can be expressed as the difference between the mean enclosed surface mass density and the surface mass density Σ at that projected radius, which is expressed as follows

$$\Sigma(R) = \int_{-\infty}^{\infty} d\chi \rho \left(\sqrt{R^2 + \chi^2} \right), \quad (6)$$

$$\langle \Sigma(< R) \rangle = \frac{2}{R^2} \int_0^R dR' R' \Sigma(R'). \quad (7)$$

Where $\rho(r)$ is the density distribution of the halo and χ is the comoving distance along the line of sight. For the shear signal induced by a halo of mass M , the average excess three-dimensional matter density is given by

$$\rho(r) = \rho_m \xi_{\text{hm}}(r|M), \quad (8)$$

where $\rho_m = \Omega_{m,0} \rho_{\text{crit},0} (1+z)^3$ is the mean matter density of the universe and $\xi_{\text{hm}}(r|M)$ is the halo-matter correlation function at the halo redshift. At small scale $\xi_{\text{hm}}(r|M)$ is dominated by the cluster density profile, the 1-halo term; at large scale, most of the contribution comes from correlated structures around the halo, referred to as the "2-halo" term. In this work, we examine both regions but focus on the 1-halo region for the cluster mass calibration.

There is a strong theoretical expectation that, barring the impact of baryonic effects, the 1-halo term region of a halo should be described by the NFW model Navarro et al. (1996, 1997). In this model, the cluster matter profile within the radius r_{200c} , which encloses a region with a mean density that is 200 times the critical density ρ_{crit} is well described as

$$\rho(r) = \delta_s \rho_{\text{crit}} \left[\frac{r}{cr_{200c}} \left(1 + \left(\frac{r}{cr_{200c}} \right)^2 \right) \right]^{-1}, \quad (9)$$

where δ_s is a characteristic overdensity depending on c , which is the halo concentration parameter. Such a halo characterized by r_{200c} has a mass which can be expressed as

$$M_{200c} = 200 \rho_{\text{crit}}(z) \frac{4\pi}{3} r_{200c}^3. \quad (10)$$

This underlying density profile implies a particular projected $\Delta\Sigma$ matter profile (Bartelmann 1996), whose amplitude scales with

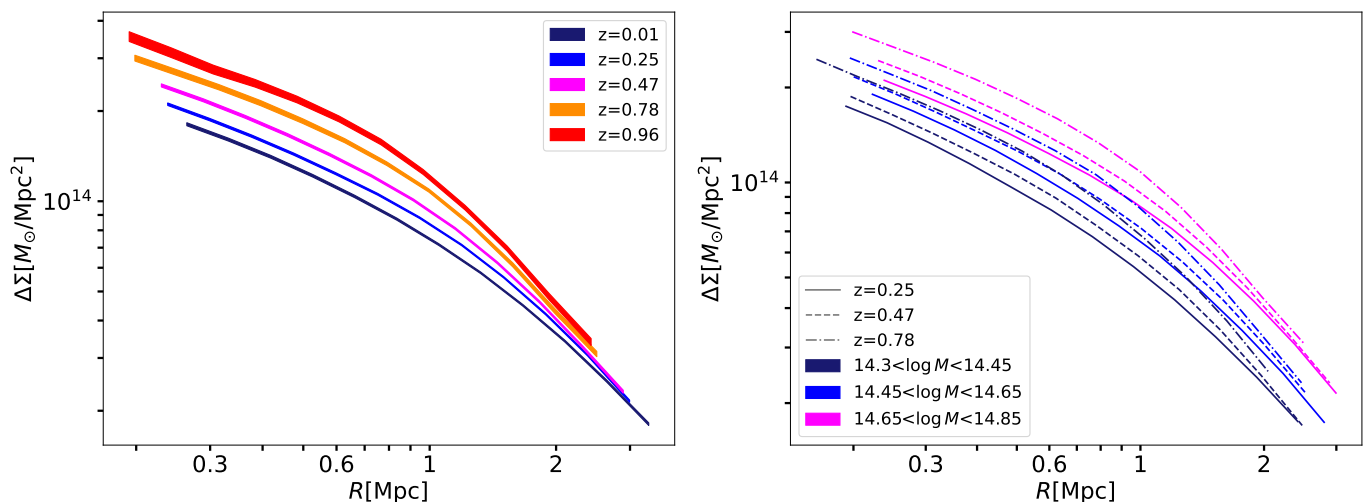


Fig. 1. Average cluster matter profiles $\Delta\Sigma(R)$ in the *Magneticum* simulation at five redshifts (color-coded on left) for the same halo-mass bin ($14.65 < \log(M_{200c}/M_{\odot}) < 14.85$) and for three mass and redshift bins (color and line-type coded on right). The dependence of the matter profiles on cluster mass and redshift is clearly visible. The thickness of the lines represents the 68% credibility region in the average matter profiles.

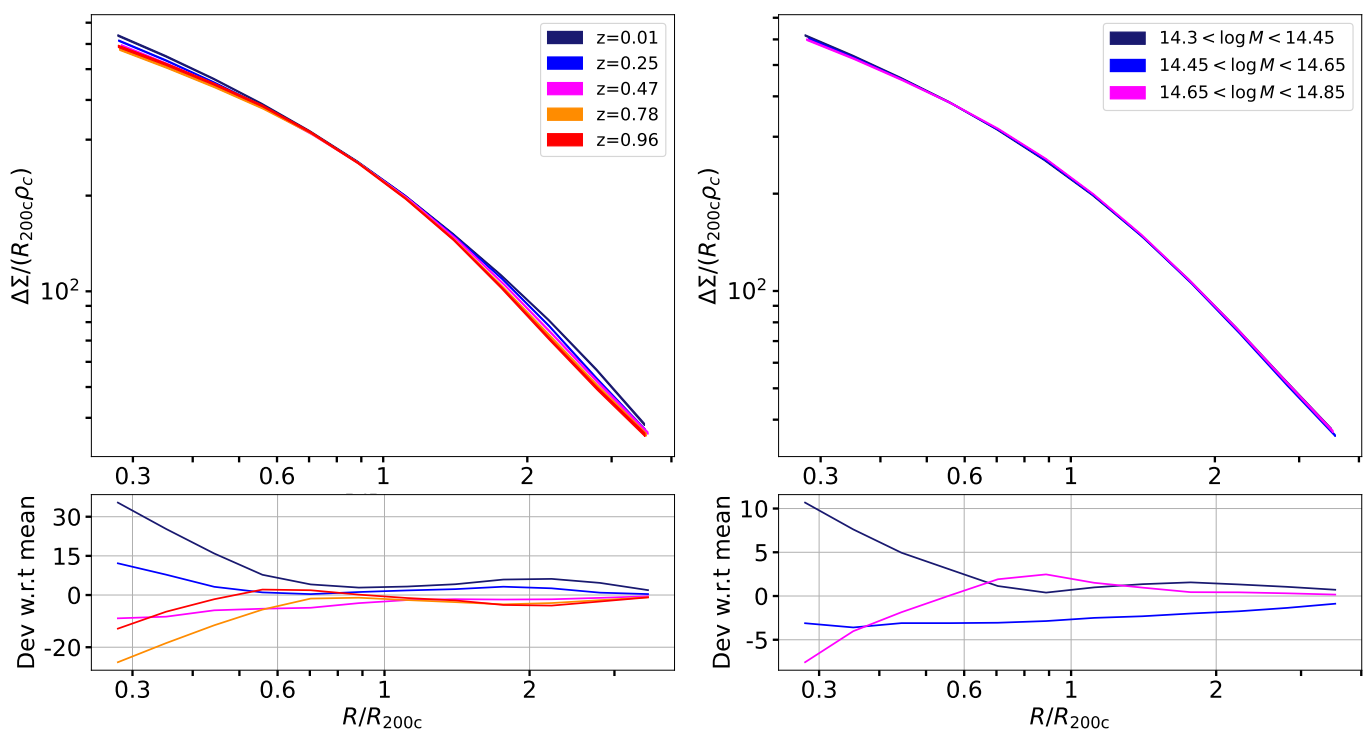


Fig. 2. Average cluster matter profiles in the *Magneticum* simulation rescaled as in Eq. (11) to $\widetilde{\Delta\Sigma}(R/R_{200c})$. In the left plot, we average all the clusters ($14.3 < \log(M_{200c}/M_{\odot}) < 15$) for a given redshift and analyze the redshift trend. In the right plot, we average clusters over all redshift ranges ($0.01 \leq z \leq 0.96$) within a mass bin and analyze the mass trends. In both panels, the bottom plot shows the deviation of individual profiles with respect to the mean of the profiles. The rescaling largely removes systematic trends in mass and redshift, highlighting the self-similar nature of the matter profiles even when baryonic components are included. The thickness of the lines in the upper panels represents the 68% credibility region in the average matter profiles.

the extent of the cluster along the line of sight (i.e., r_{200c}) and depends on the critical density, which varies with redshift as $\rho_{\text{crit}} = 3H^2(z)/8\pi G$, where $H(z)$ is the Hubble parameter at redshift z and G is the Gravitational constant. For the projected profiles discussed below, we rename r_{200c} to be R_{200c} , corresponding to the projected distance equal to the 3d radius that encloses the mass M_{200c} .

Within structure formation simulations the halo shapes vary from cluster to cluster due to formation history differences, and systematic trends in concentration with mass and redshift have

been identified (Bhattacharya et al. 2013; Covone et al. 2014). But in the limit that the systematic variation in c with mass and redshift is small, the average projected matter profiles would have the same shape in the space of R/R_{200c} . The amplitudes of these projected matter profiles would scale as $R_{200c}\rho_{\text{crit}}$. This suggests a rescaled projected matter profile $\widetilde{\Delta\Sigma}$ that would allow easy exploration of departures from self-similarity

$$\widetilde{\Delta\Sigma}\left(\frac{R}{R_{200c}}, z\right) = \frac{\Delta\Sigma\left(\frac{R}{R_{200c}}, z\right)}{R_{200c}\rho_{\text{crit}}(z)}. \quad (11)$$

We note here that for any given R_Δ , where Δ represents the overdensity with respect to the critical or mean background densities, such a rescaled $\Delta\Sigma$ profile is possible. If one chooses mean background density $\langle\rho(z)\rangle$, i.e. a scale radius of R_{200c} rather than R_{200c} , the scaling in amplitude would have to be adjusted to follow the correct redshift evolution of the mean background density $\langle\rho(z)\rangle = \Omega_m\rho_{\text{crit}}(z=0)(1+z)^3$.

Finally, because observationally determined cluster centers are not perfect tracers of the true halo center, one must consider also the impact that this mis-centering will have on the observed matter profile. When considering a mis-centering radius R_{mis} the azimuthal average of the surface mass density can be expressed as

$$\Sigma(R, R_{\text{mis}}) = \frac{1}{2\pi} \int_0^{2\pi} d\theta \Sigma \left(\sqrt{R^2 + R_{\text{mis}}^2 - 2RR_{\text{mis}}\cos\theta} \right). \quad (12)$$

Generally speaking, the mis-centering effects when using optical centers (MCMF adopts brightest cluster galaxy (BCG) position or the center of mass of the red galaxy distribution if the BCG is significantly offset from that; Klein et al. 2023) or X-ray or even SPT tSZE centers, the impact of mis-centering has only a minor impact outside the inner core region of the cluster.

3.1. Average matter profiles: hydro simulations

To enable our study of the average cluster matter profiles, we extract differential surface density cluster $\Delta\Sigma$ profiles following the method described in Grandis et al. (2021) for each redshift for both the Illustris-TNG and *Magneticum* simulations. In total, we extract 903, 852, 780, 684, and 528 cluster profiles at redshifts of 0.01, 0.25, 0.47, 0.78, and 0.96 respectively. In the absence of measurement uncertainties, we construct average $\Delta\Sigma$ profiles for further study using

$$\Delta\Sigma(R_j) = \frac{1}{N} \sum_i \Delta\Sigma_i(R_j), \quad (13)$$

where the sum is over the N clusters i in the sample and R_j is the radial binning adopted for the cluster profiles.

3.1.1. $\Delta\Sigma(R)$ dependence on mass and redshift

To start, we compute the average mass profiles for five redshifts. We compare the average matter profiles $\Delta\Sigma(R)$ at different redshifts using the *Magneticum* sample in the left panel of Fig. 1. To ensure we are seeing only trends with redshift, we average a narrow range of cluster mass ($14.65 < \log(M/M_\odot) < 14.85$) for all of the redshifts. The average cluster profiles show a significant dependence on redshift.

In the right panel of Fig. 1 we plot average matter profiles $\Delta\Sigma(R)$ at three redshifts of 0.25, 0.47, and 0.78. Each redshift bin is divided into three mass bins ($14.30 < \log(M/M_\odot) < 14.45$, $14.45 < \log(M/M_\odot) < 14.65$ and $14.65 < \log(M/M_\odot) < 14.85$). Profiles show a significant dependence on halo mass for all three redshifts. Higher mass clusters have much higher amplitude ($\Delta\Sigma(R)$ value) when compared to the low mass clusters for a given redshift due to the increased extent of the cluster along the line of sight. Averaging cluster profiles in this way will therefore lead to results that are sensitive to the distribution of the cluster sample in redshift and mass, which hampers the interpretation and characterization of such a mean matter profiles.

3.1.2. Evidence for self-similarity in mass and redshift

Motivated by the results from the previous section and the behavior of NFW profiles derived from N-body simulations, we now use the same simulated clusters to explore a rescaled matter profile $\widetilde{\Delta\Sigma}(R/R_{200c})$ (see Eq. 11) that would be the same for all samples of clusters if the population were truly self-similar.

To determine the average $\widetilde{\Delta\Sigma}$ profiles we combine the individual cluster profiles $\widetilde{\Delta\Sigma}_i$ as

$$\widetilde{\Delta\Sigma} \left(\frac{R}{R_{200c}} \right)_j = \frac{1}{N} \sum_i \widetilde{\Delta\Sigma}_i \left(\frac{R}{R_{200c}} \right)_j, \quad (14)$$

where the summation i is over the N clusters in the sample, and j denotes the radial bin in units of R/R_{200c} .

In the left panel of Fig. 2 we show average cluster profiles $\widetilde{\Delta\Sigma}(R/R_{200c})$ at five redshifts: 0.01, 0.25, 0.47, 0.78 and 0.96. We average all the clusters for a given redshift and then analyze the redshift trend. The profiles show very small variations and little change in amplitude with redshift as seen in the bottom left panel. This is in contrast to the behavior observed in Fig. 1 where we show $\Delta\Sigma(R)$. The average matter profiles line up for all redshifts from $R/R_{200c} \approx 0.6$ to $R/R_{200c} \approx 1$ with some small, remaining redshift trend at low and high R/R_{200c} .

Similarly, in the right panel of Fig. 2 we combine all the redshift samples and divide them into three mass bins ($14.30 < \log(M/M_\odot) < 14.45$, $14.45 < \log(M/M_\odot) < 14.65$ and $14.65 < \log(M/M_\odot) < 14.85$) to study the mass trends in average $\widetilde{\Delta\Sigma}(R/R_{200c})$. The profiles show remarkably small variation. This is an indication that even when hydrodynamical effects are included, simulated galaxy clusters over this range of masses and redshifts have matter profiles that exhibit strikingly similar shape. As discussed in Section 3, the lack of variation in shape is an indication of the self-similarity of cluster matter profiles along dimensions of mass and redshift.

3.1.3. Variations in average matter profiles

In this section, we aim to quantify the degree of variation we see in cluster matter profiles. For this, we calculate the fractional scatter in the average matter profiles as a function of redshift and mass. We also compare this to the fractional scatter values obtained when averaging profiles in physical space. The fractional scatter is given by $\sigma_{\Delta\Sigma}/\langle\Delta\Sigma\rangle$, where $\sigma_{\Delta\Sigma}$ is the standard deviation of the sample and $\langle\Delta\Sigma\rangle$ is the mean of the sample.

We use the *Magneticum* simulation, which has a larger volume and therefore contains many more halos in comparison to Illustris-TNG. This allows us to measure a higher SNR through averaging profiles, which in turn enables us to better quantify the intrinsic scatter in the average matter profiles. We ignore the error on average matter profiles when calculating the fractional scatter with redshift and mass on the profiles as the error is much smaller than the scatter.

Starting with the $\Delta\Sigma(R)$ profiles, we first divide each redshift bin into four mass bins. We calculate fractional scatter as a function of redshift in a given mass bin and then report the average value of fractional scatter as a function of redshift of four mass bins as a function of radius in the left panel (blue curve) of Fig. 3. The scatter ranges from $\approx 7\%$ to $\approx 19\%$ with an average of $\approx 17\%$. Similarly, when analyzing the fractional scatter as a function of mass, we compute the scatter at each redshift bin and report the mean value for five redshift bins. The orange curve in the left panel of Fig. 3 shows the mean scatter values as a function of radius R with an average of $\approx 26\%$.

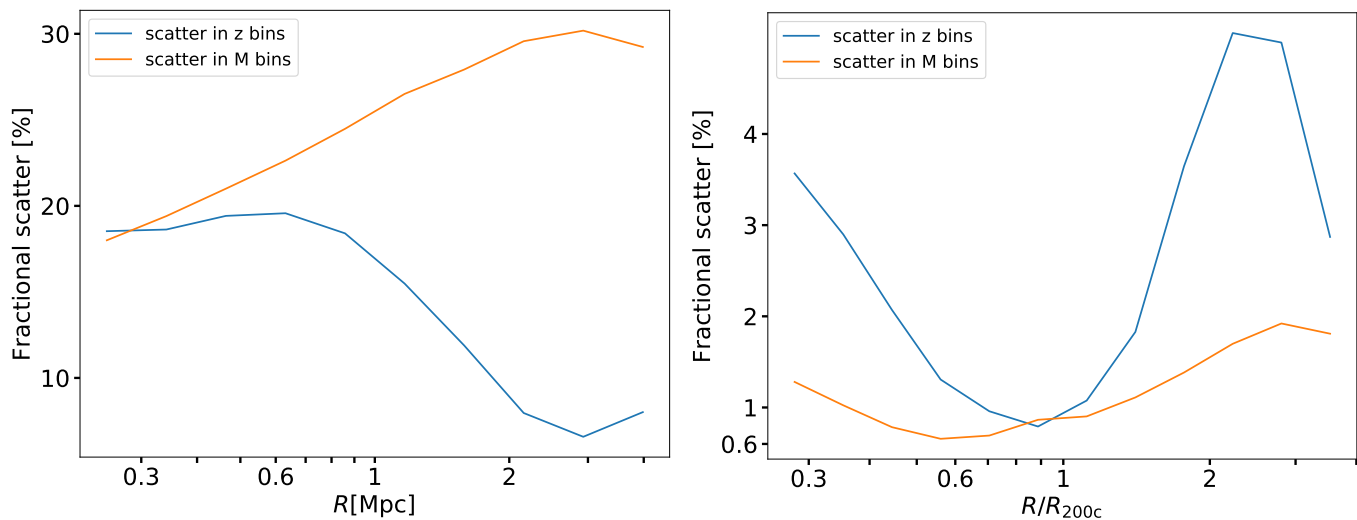


Fig. 3. The fractional variation in the average matter profiles versus radius is shown for $\Delta\Sigma(R)$ on the left and for rescaled average matter profiles $\widetilde{\Delta\Sigma}(R/R_{200c})$ on the right. We track the scatter due to redshift variations in blue and mass variations in orange. The rescaled average matter profiles exhibit a factor ≈ 6 and ≈ 23 less variation on average with redshift and mass respectively.

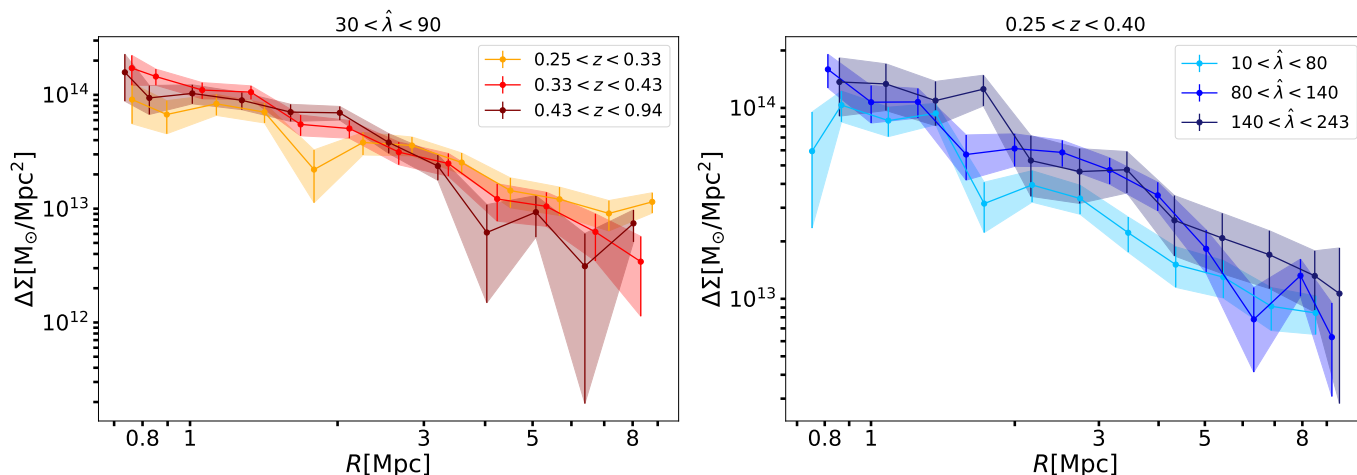


Fig. 4. SPT tSZ-selected cluster average matter profiles $\Delta\Sigma(R)$ for three redshift bins in a given richness bin, and in the right panel we show average matter profiles for different richness bins in a given redshift bin. The color bands encode the 68% credibility range for each profile. The profiles show variation with redshift and richness that is consistent with that shown in Fig. 1 for the simulated clusters.

Then moving to $\widetilde{\Delta\Sigma}(R/R_{200c})$ profiles, we average all of the clusters for a given redshift and then report the fractional scatter among the five redshift bins. The blue curve in the right panel of Fig. 3 shows the fractional scatter as a function of redshift. The value varies from $\approx 0.8\%$ to $\approx 5\%$ with an average value of $\approx 2.6\%$ and the minimum value is achieved around $\approx 0.9R/R_{200c}$. The scatter is reduced by a factor of 6 when considering $\widetilde{\Delta\Sigma}(R/R_{200c})$ in comparison to the scatter seen in $\Delta\Sigma(R)$. Similarly, when analyzing the fractional scatter as a function of mass, we divide each redshift into four mass bins and stack all of the clusters with different redshifts in a given mass bin. The orange curve in Fig. 3 shows the trend of the fractional scatter as a function of mass with scaled radius with an average value of $\approx 1.1\%$, which is 23 times smaller relative to the scatter with mass in $\Delta\Sigma(R)$.

3.2. Average matter profiles: observations

In this section, we examine the matter profiles of the 698 SPT tSZ-selected clusters using the WL data from DES in physical and rescaled space. Given the cosmological parameters \mathbf{p}

(Table 1), the average $\Delta\Sigma$ estimator for the cluster ensemble in a radial bin R_j is a triple sum over clusters k , lensing source galaxy tomographic redshift bins b and individual lensing source galaxies i as

$$\Delta\Sigma(R_j|\mathbf{p}) = \frac{\sum_{k,b,i} \frac{\Sigma_{\text{crit},k,b} w_{k,b} \mathcal{W}_{k,b,i}^s e_{l,k,b,i}}{(1-f_{\text{cl},k,b})}}{\sum_{k,b,i} w_{k,b} \mathcal{W}_{k,b,i}^s (R_{\gamma_i} + R_{\text{sel}})}. \quad (15)$$

Here \mathcal{W}_i^s are the scaled source weights, and $w_{k,b}$ are the tomographic bin weights

$$\begin{aligned} \mathcal{W}_{k,b,i}^s &= w_i^s \left(\frac{1-f_{\text{cl},k,b}}{\Sigma_{\text{crit},k,b}} \right)^2 \\ w_{k,b} &= \sum_{\text{crit},k,b}^{-1}, \end{aligned} \quad (16)$$

where the w_i^s represent individual source weights (defined as the inverse variance in the measured ellipticity). Following Bocquet et al. (2023), we employ only tomographic bins 2 to 4 in this analysis. $\Sigma_{\text{crit},k,b}$ is the critical surface density, which depends on cluster redshift and source galaxy redshift distribution, calculated as in Eq. 5. The ellipticity of a source galaxy i from a

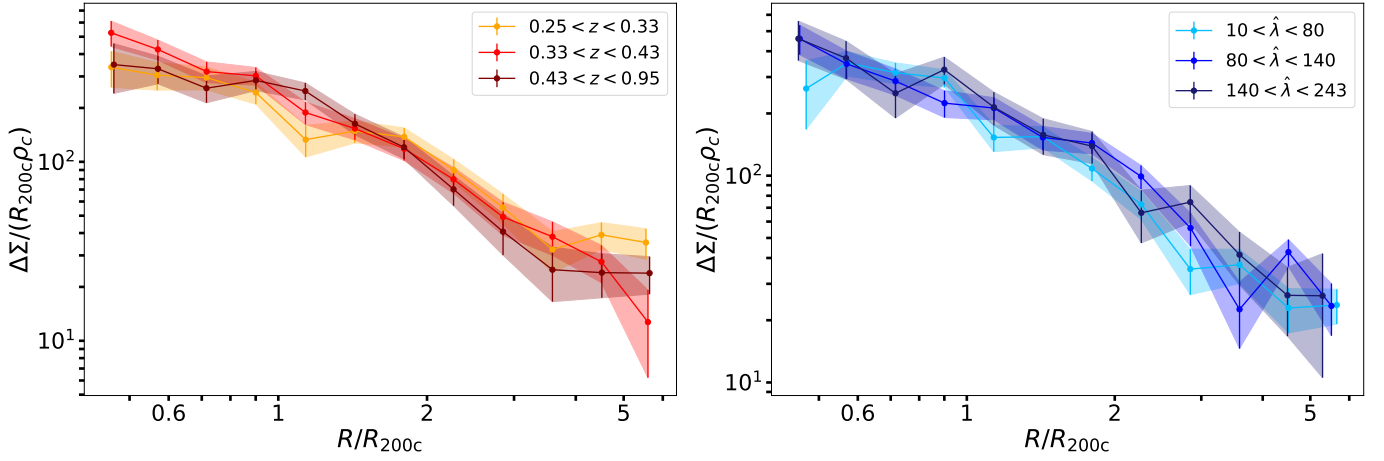


Fig. 5. Average SPT cluster profiles constructed using the mass calibration posteriors from Bocquet et al. (2024). In the left panel, we show average matter profiles $\overline{\Delta\Sigma}(R/R_{200c})$ for three redshift bins, and in the right panel are average matter profiles for different richness bins. The rescaled profiles show regularity similar to that seen in Fig. 2 for the cluster simulations.

tomographic bin b and lying in the background of a cluster k is $e_{t,k,b,i}$, and $R_{\gamma,i}$ is the shear response for galaxy i , which is needed to scale the ellipticity to the reduced shear. Additionally, the selection response R_{sel} accounts for the fact that lensing sources are selected based on their (intrinsically) sheared observations. We use $R_{\text{sel}} = -0.0026$ for optical centers as measured previously for this sample (Bocquet et al. 2023). We also scale the ellipticity with a factor of $1/(1-f_{\text{cl},k,b})$ to correct the profiles for the cluster member contamination, which is measured separately for each tomographic redshift bin (see discussion in Section 4.4).

The corresponding uncertainty in $\Delta\Sigma$ for a radial bin R_j in the average cluster profile is calculated as

$$\sigma_{\Delta\Sigma}^2(R_j|\mathbf{p}) = \frac{\sum_{k,b,i} \left(\frac{\Sigma_{\text{crit},k,b} w_{k,b} \overline{W}_{k,b,i}^s \sigma_{\text{eff},b}}{(1-f_{\text{cl},k,b})} \right)^2}{\left(\sum_{k,b,i} w_{k,b} \overline{W}_{k,b,i}^s \right)^2}. \quad (17)$$

Here $\sigma_{\text{eff},b}^2$ is the effective shape variance for sources in a given tomographic bin, and all other elements are as described in Eq. 15.

Similarly, after accounting for the rescaling described in Eq. 11 and given the cosmological parameters \mathbf{p} and the cluster radii \mathbf{M}_{200c} the average $\overline{\Delta\Sigma}$ estimator in a radial bin $(R/R_{200c})_j$ is given by

$$\overline{\Delta\Sigma} \left(\frac{R}{R_{200c}} \middle| \mathbf{M}_{200c}, \mathbf{p} \right)_j = \frac{\sum_{k,b,i} \frac{\Sigma_{\text{crit},k,b} w_{k,b} \overline{W}_{k,b,i}^s e_{t,k,b,i}}{\rho_{\text{crit},k} R_{200c,k} (1-f_{\text{cl},k,b})}}{\sum_{k,b,i} w_{k,b} \overline{W}_{k,b,i}^s (R_{\gamma,i} + R_{\text{sel}})}, \quad (18)$$

where $\overline{W}_{k,b,i}^s$ is the re-scaled source weight which is defined as

$$\overline{W}_{k,b,i}^s = w_i^s \left(\frac{\rho_{\text{crit},k} R_{200c,k} (1-f_{\text{cl},k,b})}{\Sigma_{\text{crit},k,b}} \right)^2, \quad (19)$$

and the corresponding uncertainty is given by

$$\sigma_{\overline{\Delta\Sigma}}^2 \left(\frac{R}{R_{200c}} \middle| \mathbf{M}_{200c}, \mathbf{p} \right)_j = \frac{\sum_{k,b,i} \left(\frac{\Sigma_{\text{crit},k,b} w_{k,b} \overline{W}_{k,b,i}^s \sigma_{\text{eff},b}}{\rho_{\text{crit},k} R_{200c,k} (1-f_{\text{cl},k,b})} \right)^2}{\left(\sum_{k,b,i} w_{k,b} \overline{W}_{k,b,i}^s \right)^2}. \quad (20)$$

The mean estimated scaled radius of a given radial bin j is calculated from the equation

$$\left(\frac{R}{R_{200c}} \middle| \mathbf{M}_{200c}, \mathbf{p} \right)_j = \frac{\sum_{k,b,i} w_{k,b} \overline{W}_{k,b,i}^s R_{k,b,i} / R_{200c,k}}{\sum_{k,b,i} w_{k,b} \overline{W}_{k,b,i}^s}, \quad (21)$$

where $R_{k,b,i}$ is the projected separation of ellipticity i in tomographic bin b from the center of cluster k . A similar expression for the mean radius R_j within a bin pertains, but without the $1/R_{200c}$ scaling.

In the left panel of Fig. 4 we show the average cluster profile $\Delta\Sigma(R)$, in three redshift bins (for a richness bin, $30 < \lambda < 90$ containing 426 clusters), and in the right panel, we show the average cluster profiles in three richness bins (for a redshift bin, $0.25 < z < 0.40$ containing 123 clusters). While the measurement uncertainties are significant in this sample (color bands represent 68% credibility regions), it is still possible to discern variations among the presented average matter profiles.

To study the average $\overline{\Delta\Sigma}(R/R_{200c})$ profiles, we need a robust value of R_{200c} for each cluster, which then implies we need good mass constraints for each system (Eq. 10). For this purpose, we adopt the observable-mass relation (ζ -mass and λ -mass— see discussion in Section 4.1) posteriors from Bocquet et al. (2024), where the mass calibration constraints were obtained using the same DES WL data as part of the cosmological cluster abundance analysis of the sample (Bocquet et al. 2023). We use the full sample while analyzing clusters in redshift or richness bins. The rescaled average cluster matter profiles exhibit much less evidence for variation than the $\Delta\Sigma(R)$ profiles in Fig. 4. In other words, the tSZE selected clusters show indications of self-similarity with redshift and richness similar to those presented above for the clusters from hydrodynamical simulations.

This simplicity in the rescaled average matter profiles $\overline{\Delta\Sigma}(R/R_{200c})$ of the simulated and observed galaxy cluster population offers some advantages. It allows us to combine large ensembles of clusters with a wide halo mass and redshift range, creating higher SNR cluster matter profiles, which can be used to test different models of structure formation. Moreover, the modeling of average cluster profiles $\overline{\Delta\Sigma}(R/R_{200c})$ for observed cluster samples becomes straightforward. We employ this simplicity in matter profiles in Section 4, where we present a new method of galaxy cluster mass calibration that exploits the approximate self-similarity of galaxy clusters.

4. Mass Calibration Method

Measurements of the weak lensing signal induced by foreground galaxy clusters can be used to robustly estimate the cluster mass. However, because the SNR of the WL signal is low for individual

clusters, it is practical to perform mass calibration using the lensing signal averaged over many clusters (e.g. Umetsu et al. 2014, 2016; Okabe et al. 2010, 2013). Because the rescaled average matter profiles $\widetilde{\Delta\Sigma}(R/R_{200c})$ are particularly simple to model, they offer the possibility to improve upon previous average matter profile based weak lensing mass calibration methods.

This method presented below involves 1) building an ensemble of rescaled average matter profiles— one for each bin in cluster observable, 2) extracting a likelihood of consistency between these matter profiles and a model profile and then 3) iterating with a Markov Chain Monte Carlo method to characterize the posteriors of the model parameters. These parameters describe the galaxy cluster observable–mass relations discussed in Section 4.1. The mean posteriors describe the parameters for which the observed and model average matter profiles are consistent over the full range of cluster observables. The average matter profile model is discussed in Section 4.2, and the mass calibration likelihood is presented in Section 4.3. A discussion of the systematic effects and their correction then appears in Section 4.4.

4.1. Observable-mass relations

In our analysis, each confirmed cluster has four associated observable quantities. These include the tSZE detection significance $\hat{\zeta}$, the MCMF obtained richness $\hat{\lambda}$ and redshift z and the weak lensing mass M_{WL} that is derived using weak lensing shear and photometric redshift data of the background lensed galaxies. The weak lensing masses are measured using average matter profiles $\widetilde{\Delta\Sigma}(R/R_{200c})$, and these masses are used to constrain the so-called cluster observable–mass relations (e.g. Mohr & Evrard 1997; Mohr et al. 1999; Finoguenov et al. 2001; Chiu et al. 2016, 2018; Bulbul et al. 2019) that describe the redshift dependent statistical binding between the observables (i.e., detection significance, richness and weak lensing mass) and the underlying halo mass M_{200c} .

4.1.1. tSZE detection significance $\hat{\zeta}$

The tSZE detection significance $\hat{\zeta}$ is related to the unbiased significance ζ as

$$P(\hat{\zeta}|\zeta) = \mathcal{N}\left(\sqrt{\zeta^2 + 3}, 1\right). \quad (22)$$

This relationship accounts for the maximization bias in $\hat{\zeta}$ caused during the cluster matched filter candidate selection (Melin et al. 2006), which has three free parameters (cluster sky location and cluster model filter scale). The normal distribution models the impact of the unit noise in the appropriately rescaled mm-wave maps. The mean unbiased detection significance is modeled as a power-law relation in mass and redshift

$$\langle \ln \zeta | M_{200c}, z \rangle = \ln \zeta_0 + \zeta_M \ln \left(\frac{M_{200c}}{M_{\text{piv}}} \right) + \zeta_z \ln \left(\frac{E(z)}{E(z_{\text{piv}})} \right), \quad (23)$$

where $E(z)$ is the dimensionless Hubble parameter, $M_{\text{piv}} = 3 \times 10^{14} h^{-1} M_{\odot}$ is the pivot mass and $z_{\text{piv}} = 0.6$ is the pivot redshift, which are chosen to reflect the median mass and redshift of our SPT catalog. To account for the variable depth of the SPT survey fields, we rescale the amplitude ζ_0 on a field-by-field basis

$$\zeta_{0,i} = \gamma_i \zeta_0, \quad (24)$$

where γ_i is obtained from simulated maps (Bleem et al. 2015; Bleem et al. 2020, 2023). This approach allows us to combine the full SPT cluster sample when empirically modeling the ζ -mass relation. We model the intrinsic scatter in ζ at fixed mass and redshift as log-normal $\sigma_{\ln \zeta}$. This single scatter parameter has been shown to be sufficient to model the SPT tSZE-selected cluster sample ζ -mass relation (Bocquet et al. 2019; Bocquet et al. 2024).

4.1.2. Cluster richness $\hat{\lambda}$

The observed cluster richness $\hat{\lambda}$ is related to the intrinsic richness λ as

$$P(\hat{\lambda}|\lambda) = \mathcal{N}\left(\lambda, \sqrt{\lambda}\right), \quad (25)$$

which models the Poisson sampling noise in the limit of a normal distribution where the dispersion is $\sigma = \sqrt{\lambda}$. The mean intrinsic richness is modeled as a power law in mass and redshift

$$\langle \ln \lambda | M_{200c}, z \rangle = \ln \lambda_0 + \lambda_M \ln \left(\frac{M_{200c}}{M_{\text{piv}}} \right) + \lambda_z \ln \left(\frac{1+z}{1+z_{\text{piv}}} \right), \quad (26)$$

where as above $M_{\text{piv}} = 3 \times 10^{14} h^{-1} M_{\odot}$ and $z_{\text{piv}} = 0.6$. The intrinsic scatter of the intrinsic richness λ at fixed mass and redshift is modeled as a log-normal distribution with the parameter $\sigma_{\ln \lambda}$. This scatter is the same for all redshifts and masses, which has been shown to be adequate for modeling the λ -mass relation of the SPT selected cluster sample (Bocquet et al. 2024).

4.1.3. Weak lensing mass M_{WL}

In addition to the ζ -mass and λ -mass relations, we also include a mapping between the so-called weak lensing mass M_{WL} , which is the mass one would infer by fitting a model profile to an individual cluster matter profile. This follows the approach adopted in previous work (Becker & Kravtsov 2011; Dietrich et al. 2019; Grandis et al. 2021; Bocquet et al. 2023) and is a mechanism for incorporating corrections for systematic biases that may arise from the interpretation of the average matter profiles and for marginalising over the remaining systematic uncertainties in those bias corrections. For example, the uncertainties associated with hydrodynamical simulations and the subgrid physics they incorporate can be modeled with this M_{WL} -mass relation, incorporating an effective systematic floor in the accuracy of the final, calibrated masses. We characterize this relation as

$$\left\langle \ln \left(\frac{M_{\text{WL}}}{M_{\text{piv}}} \right) \right\rangle = \ln M_{\text{WL}_0} + M_{\text{WL}_M} \ln \left(\frac{M_{200c}}{M_{\text{piv}}} \right) + M_{\text{WL}_z} \ln \left(\frac{1+z}{1+z_{\text{piv}}} \right), \quad (27)$$

where $\ln M_{\text{WL}_0}$ is the logarithmic bias at $M_{200c} = M_{\text{piv}}$ and M_{WL_M} and M_{WL_z} are the mass and redshift trends of this bias. Here we explicitly include the redshift trend parametrization, whereas in previous analyses (see Bocquet et al. 2023) the relation was defined at specific redshifts where the required simulations were available.

The weak lensing mass M_{WL} estimated from individual clusters exhibits a mass dependent log-normal scatter $\sigma_{\ln \text{WL}}$ about the mean relation, which we model as

$$\ln \sigma_{\ln \text{WL}}^2 = \ln \sigma_{\ln \text{WL}_0}^2 + \sigma_{\ln \text{WL}_M}^2 \ln \left(\frac{M_{200c}}{M_{\text{piv}}} \right) + \sigma_{\ln \text{WL}_z}^2 \ln \left(\frac{1+z}{1+z_{\text{piv}}} \right), \quad (28)$$

where $\ln \sigma_{\ln M_{\text{WL}_0}}^2$ is the logarithm of the variance of M_{WL} around M_{200c} at M_{piv} and $\sigma_{\ln M_{\text{WL}_M}}^2$ and $\sigma_{\ln M_{\text{WL}_z}}^2$ are the mass and redshift trends of this variance. For an average rescaled matter profile that is produced using N clusters, the effective scatter of the extracted M_{WL} about the true mass would scale down as $1/\sqrt{N}$, reducing the stochasticity associated with the estimate of the underlying halo mass and reducing the importance of possible correlations between the scatter in M_{WL} and other observables.

In general, the parameter posteriors on these relations are extracted through a M_{WL} calibration exercise carried out on hydrodynamical simulations of clusters output over a range of redshifts (Grandis et al. 2021). This calibration exercise employs a model profile or set of model profiles as discussed in the next section and characterizes the biases and scatter associated with that model. In addition, systematic uncertainties on photometric redshifts, the multiplicative shear bias, the cluster member contamination model and the cluster mis-centering model are also incorporated into the posteriors on these parameters, making it straightforward to marginalize over all critical systematic uncertainties in the mass calibration analysis. We return to this in Section 4.4.

4.2. Average rescaled matter profile model $\widetilde{\Delta\Sigma}_{\text{mod}}$

We use the Illustris-TNG and the *Magneticum* simulations at five redshifts between 0 to 1 (as described in the Section 2.3) to create an average weak lensing model for use in mass calibration. Because there is little variation in the average matter profiles $\widetilde{\Delta\Sigma}(R/R_{200c})$ with mass and redshift, we could adopt a single average matter profile at all redshifts and masses for the model used in mass calibration. We could then correct for the small biases introduced by this assumption of perfect self-similarity using the M_{WL} -mass relations (Eq. 27 and 28). However, an examination of the average matter profiles presented in Fig. 2 provides clear evidence for small departures from self-similarity with redshift, while showing no convincing evidence of departures from self-similarity in mass. Therefore, we adopt a model $\widetilde{\Delta\Sigma}(R/R_{200c})$ profile that varies with redshift, while assuming perfect self-similarity in mass. This essentially sets the mean logarithmic bias $\ln M_{\text{WL}_0}$ in the M_{WL} -mass relation to zero over all masses and redshifts.

Illustris-TNG contains 301, 284, 260, 228, and 176 halos corresponding to the redshifts 0.01, 0.24, 0.42, 0.64, and 0.95, respectively. Because the subgrid physics is different in the two sets of simulations, the average matter profiles from the two sets of simulations need not be the same. To create the average weak lensing model that is representative of the typical behavior of the two sets of simulations, we therefore select the same number of simulated clusters from the *Magneticum* simulation. We randomly choose 301, 284, 260, 228, and 176 halos corresponding to the redshifts 0.01, 0.25, 0.47, 0.78, 0.96, respectively, from *Magneticum*.

For each halo, we extract 3 mis-centered cluster profiles (using the method described in Grandis et al. (2021)) and average all of the clusters at a given redshift from both simulations. We follow the mis-centering distribution model as described in the Section 4.4.1. Because mis-centering depends on the richness of the cluster, we assign each halo a richness value using the richness-mass relation (Eq. 26) using the parameters obtained in a previous cluster cosmology analysis (Chiu et al. 2023). These individual $\Delta\Sigma(R)$ profiles are then rescaled into $\widetilde{\Delta\Sigma}(R/R_{200c})$ profiles and averaged following Eq. 14.

Given that the two sets of simulations do not have outputs at exactly the same redshifts, e.g., 0.42 vs. 0.47 and 0.64 vs. 0.78, we quantify the differences in the average $\widetilde{\Delta\Sigma}(R/R_{200c})$ profiles at these redshifts, verifying that this induces a negligible uncertainty. This is achieved by interpolating the profiles from both simulations as a function of redshift separately and comparing for each simulation the differences in the profiles at both the redshifts, and finding them to be very small (percentage error of $\approx 0.4\%$, see Fig. A.1). We therefore adopt the mean value of the redshift (in case the redshifts are different) while combining the profiles from both simulations. The combined profiles are then interpolated as a function of redshift to capture the slight differences we see with redshift in the average $\widetilde{\Delta\Sigma}(R/R_{200c})$ profiles.

Once an average rescaled matter profile model has been chosen, it is used to characterize the bias and scatter in the M_{WL} estimates with respect to the true underlying halo masses, determining posteriors of the parameters in Eq. 27 and 28. As part of this calibration process, uncertainties on the other crucial systematics (uncorrelated large-scale structure covariance, cluster mis-centering, cluster member contamination of the source galaxy sample, and hydrodynamical uncertainties on the model) are also included.

4.3. Mass calibration likelihood

In this section, we present the mass calibration likelihood that we employ with the average rescaled matter profile $\widetilde{\Delta\Sigma}(R/R_{200c})$. The lowest level observational constraint from weak gravitational lensing is a tangential reduced shear profile (Eq. 1) constructed for each of a series of tomographic bins within which the shear galaxy sample is organized. A complication with using the tangential shear profiles (see, e.g., Bocquet et al. 2023), is that the profiles from the different bins cannot be averaged, because the amplitude depends on Σ_{crit} , which depends on the redshift distributions of the background galaxies (Eq. 4). The matter profile $\Delta\Sigma(R)$ (Eq. 3) is simpler in that the profiles for each tomographic bin are all estimators of the same underlying projected matter density of the cluster (see, e.g., McClintock et al. 2018). The observable we adopt here $\widetilde{\Delta\Sigma}(R/R_{200c})$ (Eq. 11) offers additional simplicity, because this profile is approximately the same for all clusters, independent of their mass and redshift. However, the matter profile $\Delta\Sigma(R)$ and rescaled matter profile $\widetilde{\Delta\Sigma}(R/R_{200c})$ are no longer pure observables. They both have dependences on cosmological parameters that impact the distance-redshift relation, and the rescaled matter profile also has dependences on the masses and redshifts of the constituent clusters. This dependence has to be considered within the likelihood, as outlined in the next subsection.

4.3.1. Rescaled matter profile likelihood

The lensing likelihood for an average rescaled matter profile is given by a product of the independent Gaussian probabilities of obtaining the observed matter profile given the model within each radial bin. Because the rescaled matter profile $\widetilde{\Delta\Sigma}(R/R_{200c})$ depends on cosmological parameters and the masses and radii of the constituent clusters, the likelihood has to be altered to account for these dependencies. The likelihood transformation for a data vector t_θ which is some function of a data vector y (independent of model parameters) and model parameters θ is

given by (Severini 2004)

$$P(t_\theta|\theta)d\theta \longrightarrow P(t_\theta|\theta)\left|\frac{\partial t_\theta}{\partial \mu}\right|d\mu. \quad (29)$$

Here μ denotes a function of data y that has the same dimension as t_θ and is independent of the model parameters θ . In the case where μ cannot be expressed with the same dimension as t_θ , the likelihood transformation is then given by

$$P(t_\theta|\theta)d\theta \longrightarrow P(t_\theta|\theta)\left|\frac{\partial t_\theta}{\partial \mu}\left(\frac{\partial t_\theta}{\partial \mu}\right)^T\right|^{1/2}d\mu. \quad (30)$$

Using Eq. 30 we can write the transformed Gaussian likelihood (lensing likelihood) for a rescaled matter profile $\widetilde{\Delta\Sigma}(M_{200c}, \mathbf{p})$ (given by Eq. 18) with i radial bins as

$$P(\widetilde{\Delta\Sigma}(M_{200c}, \mathbf{p})|\widetilde{\Delta\Sigma}_{\text{mod}}, z) = P_G \prod_i \left(\left| \frac{\partial \widetilde{\Delta\Sigma}_i}{\partial \mathbf{e}_{t,i}} \left(\frac{\partial \widetilde{\Delta\Sigma}_i}{\partial \mathbf{e}_{t,i}} \right)^T \right|^{1/2} \right), \quad (31)$$

where the second factor in the above equation is the transformation calculation for all the radial bins, $\mathbf{e}_{t,i} = [e_{t,i}^1, e_{t,i}^2, e_{t,i}^3 \dots e_{t,i}^n]$ is the vector containing the n source ellipticities in a given radial bin i and P_G is the Gaussian likelihood defined as

$$P_G = \prod_i \left(\sqrt{2\pi} \sigma_{\widetilde{\Delta\Sigma},i} \right)^{-1} \exp \left[-\frac{1}{2} \left(\frac{\widetilde{\Delta\Sigma}_i - \widetilde{\Delta\Sigma}_{\text{mod},i}}{\sigma_{\widetilde{\Delta\Sigma},i}} \right)^2 \right], \quad (32)$$

where $\widetilde{\Delta\Sigma}_{\text{mod}}$ is the model profile and $\sigma_{\widetilde{\Delta\Sigma},i}$ is the rescaled shape noise as described in Eq. 20. The likelihood transformation is a 1-dimensional partial derivative matrix with length n and is given by

$$\frac{\partial \widetilde{\Delta\Sigma}_i}{\partial \mathbf{e}_{t,i}} = \left[\frac{\partial \widetilde{\Delta\Sigma}_i}{\partial e_{t,i}^1}, \frac{\partial \widetilde{\Delta\Sigma}_i}{\partial e_{t,i}^2}, \dots, \frac{\partial \widetilde{\Delta\Sigma}_i}{\partial e_{t,i}^n} \right]. \quad (33)$$

The transformation factor can then be expressed as

$$\left| \frac{\partial \widetilde{\Delta\Sigma}_i}{\partial \mathbf{e}_{t,i}} \left(\frac{\partial \widetilde{\Delta\Sigma}_i}{\partial \mathbf{e}_{t,i}} \right)^T \right|^{1/2} = \left(\frac{\partial \widetilde{\Delta\Sigma}_i}{\partial e_{t,i}^1}^2 + \frac{\partial \widetilde{\Delta\Sigma}_i}{\partial e_{t,i}^2}^2 + \dots + \frac{\partial \widetilde{\Delta\Sigma}_i}{\partial e_{t,i}^n}^2 \right)^{1/2}. \quad (34)$$

4.3.2. Single cluster rescaled matter profile likelihood

The intrinsic scatter in the observable mass relations, the measurement noise on the observables, the uncertainties on the observable-mass relation parameters and the uncertainties on the cosmological parameters all contribute to create the posterior mass distribution $P(M|\hat{\zeta}, \hat{\lambda}, z, \mathbf{p})$ for a given cluster. Even in the limit of perfect knowledge of the scaling relation and cosmological parameters, this posterior distribution has some characteristic width determined by the mass trends in each observable together with the sources of scatter mentioned above. Moreover, even in the case of a perfect match between the observed and model rescaled matter profiles, the resulting weak lensing mass estimate is a biased and scattered estimator of the true halo mass M_{200c} as constrained in the M_{WL} -halo mass relations (Eq. 27 and 28).

The cluster mass uncertainty represented by this mass posterior and any biases and scatter in the weak lensing mass estimate have to be accounted for. Therefore, the single cluster lensing likelihood for cluster k with the weak lensing mass posterior

$P_k(M_{\text{WL}}|\hat{\zeta}, \hat{\lambda}, z, \mathbf{p})$ and rescaled matter profile $\widetilde{\Delta\Sigma}_k$ is written as

$$P(\widetilde{\Delta\Sigma}_k|\widetilde{\Delta\Sigma}_{\text{mod}}, z) = \int dM_{\text{WL}} P_k(M_{\text{WL}}|\hat{\zeta}, \hat{\lambda}, z, \mathbf{p}) P(\widetilde{\Delta\Sigma}_k(M_{\text{WL}})|\widetilde{\Delta\Sigma}_{\text{mod}}, z), \quad (35)$$

where we are explicit with subscript k to emphasize that this expression represents a weighted likelihood for a single cluster. We note that the M_{WL} dependence of $\widetilde{\Delta\Sigma}_k$ is due to the cluster radius (Eq. 11), which is mass dependent as in Eq. 10.

We calculate the mass posterior using three observables $\hat{\zeta}$, $\hat{\lambda}$ and z (we neglect the cluster photometric redshift uncertainty since it is too small relative to other sources of scatter to be important). The general Bayes theorem expression for the mass posterior of a cluster that accounts for intrinsic and measurement scatter in the observables is

$$P(M_{\text{WL}}|\hat{\zeta}, \hat{\lambda}, z, \mathbf{p}) = \frac{\iiint dM d\lambda d\zeta P(\hat{\lambda}|\lambda) P(\hat{\zeta}|\zeta) P(\zeta, \lambda, M_{\text{WL}}|M, z, \mathbf{p}) P(M|z, \mathbf{p})}{P(\hat{\lambda}, \hat{\zeta}|z, \mathbf{p})}, \quad (36)$$

where the measurement noise is represented by $P(\hat{\lambda}|\lambda)$ and $P(\hat{\zeta}|\zeta)$, the intrinsic scatter and any bias in the observable about mass by $P(\zeta, \lambda, M_{\text{WL}}|M, z, \mathbf{p})$, $P(M|z, \mathbf{p})$ is the halo mass function and $P(\hat{\lambda}, \hat{\zeta}|z, \mathbf{p})$ is just the numerator integrated over M_{WL} .

In the context of multiple observables, the single cluster mass calibration likelihood $\mathcal{L}_{\text{single}}$ can be written (assuming $\widetilde{\Delta\Sigma}$ is uncorrelated with other observables) as a product of the single cluster lensing likelihood and the likelihood of the observables

$$\mathcal{L}_{\text{single}} = P(\widetilde{\Delta\Sigma}_k|\widetilde{\Delta\Sigma}_{\text{mod}}, z) P(\hat{\lambda}, \hat{\zeta}, z, \mathbf{p}), \quad (37)$$

where the second component is the likelihood of observed richness $\hat{\lambda}$ given the observed tSZE detection significance $\hat{\zeta}$ and redshift z . It can be calculated using Bayes theorem accounting for intrinsic scatter in the observables

$$P(\hat{\lambda}|\hat{\zeta}, z, \mathbf{p}) = \frac{\iiint dM d\lambda d\zeta P(\hat{\lambda}|\lambda) P(\hat{\zeta}|\zeta) P(\zeta, \lambda|M, z, \mathbf{p}) P(M|z, \mathbf{p})}{P(\hat{\zeta}|z, \mathbf{p})}, \quad (38)$$

where $P(\hat{\zeta}|z, \mathbf{p})$ is just the normalization that comes from integrating the numerator over all $\hat{\lambda}$, which is crucial for accounting Malmquist bias.

4.3.3. Multi-cluster average rescaled matter profile likelihood

For a given $\hat{\zeta} - \hat{\lambda} - z$ bin containing n clusters, the rescaled matter profile $\widetilde{\Delta\Sigma}$ is notionally calculated as in Eq. 18. However, as discussed above for the single cluster rescaled matter profile, the mass posteriors of the clusters must be included. Rather than extracting an average likelihood by marginalizing over the weak lensing mass posterior $P(M_{\text{WL}}|\hat{\zeta}, \hat{\lambda}, z, \mathbf{p})$ as in the single cluster case (Eq. 35), in the multi-cluster case we adopt a Monte Carlo integration approach that allows us to efficiently marginalize over the mass posteriors of all n clusters simultaneously. In effect, we rebuild the average matter profile $\widetilde{\Delta\Sigma}$ for the cluster ensemble many times and use those profiles to extract likelihoods and then estimate the average likelihood of the rescaled matter profile.

Following the likelihood for a single cluster profile in Eq. 37, we write the weak lensing mass calibration likelihood for an ensemble of n clusters with associated observables, $M_{\text{WL},i}$, $\hat{\lambda}_i$, $\hat{\zeta}_i$ and z_i as

$$\mathcal{L}_{\text{bin}} = \langle P(\widetilde{\Delta\Sigma}(\mathbf{M}_{\text{WL}}, \mathbf{p}) | \widetilde{\Delta\Sigma}_{\text{mod}}, \mathbf{z}) \prod_{i=1}^n P(\hat{\lambda}_i | \hat{\zeta}_i, z_i, \mathbf{p}), \quad (39)$$

where $\langle P(\widetilde{\Delta\Sigma}(\mathbf{M}_{\text{WL}}, \mathbf{p}) | \widetilde{\Delta\Sigma}_{\text{mod}}, \mathbf{z}) \rangle$ is the average lensing likelihood of the average rescaled matter profile built from the ensemble. The observable vectors \mathbf{M}_{WL} , $\hat{\lambda}$, $\hat{\zeta}$, and \mathbf{z} each contain the n measurements for the clusters in the ensemble. For an n cluster ensemble, it takes the form

$$\begin{aligned} \langle P(\widetilde{\Delta\Sigma}(\mathbf{M}_{\text{WL}}, \mathbf{p}) | \widetilde{\Delta\Sigma}_{\text{mod}}, \mathbf{z}) \rangle = \\ \int \cdots \int dM_{\text{WL}_1} \cdots dM_{\text{WL}_n} P(M_{\text{WL}_1} | \hat{\zeta}_1, \hat{\lambda}_1, z_1, \mathbf{p}) \times \cdots \\ P(M_{\text{WL}_n} | \hat{\zeta}_n, \hat{\lambda}_n, z_n, \mathbf{p}) \\ P(\widetilde{\Delta\Sigma}(M_{\text{WL}_1}, \dots, M_{\text{WL}_n}, \mathbf{p}) | \widetilde{\Delta\Sigma}_{\text{mod}}, \mathbf{z}), \quad (40) \end{aligned}$$

where we note that the \mathbf{M}_{WL} is needed to build the rescaled matter profile (using Eq. 18 with \mathbf{M}_{WL} instead of \mathbf{M}_{200c}) and is calculated from observables ($\hat{\lambda}$, $\hat{\zeta}$ and \mathbf{z}) and M_{WL} -mass relation using Eq. 27.

The final likelihood for m $\hat{\zeta} - \hat{\lambda} - z$ bins can be written as the product of the likelihood of individual bins

$$\mathcal{L} = \prod_{\text{bin}=1}^m \mathcal{L}_{\text{bin}}. \quad (41)$$

4.4. Modeling and correcting for systematic effects

4.4.1. Mis-centering distribution

For each of the clusters in our sample, we have two measurements of the cluster center. The first is the tSZE center as measured by the SPT and the second is the optical center extracted using the MCMF algorithm. MCMF adopts the BCG as the center if it is within 250 kpc of the cluster position determined by SPT; otherwise, the position of the peak of the galaxy density map is used. We only make use of MCMF centers for our analysis. As the observationally determined center is not a perfect tracer of the true halo center, the effect of this mis-centering must be taken into account when modeling the cluster lensing profile. We adopt the mis-centering model and the parameters from the recent work by Bocquet et al. (2023). The mis-centering distribution for the tSZE and optical centers is modeled using the double Rayleigh distribution.

$$\begin{aligned} P_{\text{offset}}(r) = \rho \text{Rayl}(r, \sigma_0) + (1 - \rho) \text{Rayl}(r, \sigma_1), \\ \sigma_i = \sigma_{i,0} \left(\frac{\lambda}{60} \right)^{1/3} \text{ for } i \in \{0, 1\}. \quad (42) \end{aligned}$$

The double Rayleigh distribution is a good description of the mis-centering of the optical center with respect to the true halo center. The constraints on the mis-centering parameters (ρ , σ_0 , σ_1) are obtained by simultaneously fitting for SPT and optical centers. A large fraction of clusters ($\rho \approx 0.89$) are well centered with $\sigma_0 \approx 0.007$ and $\sigma_1 \approx 0.19$ (Bocquet et al. 2023).

Crucial for our mass calibration analysis is to include the effects of uncertainties on the mis-centering distribution. We do this as part of the M_{WL} -mass relation calibration. However, given the radial range we adopt for mass calibration ($R > 500h^{-1}$ kpc), the miscentering itself and the uncertainties on the mis-centering have little impact on our results.

4.4.2. Cluster member contamination

Due to the uncertainty in the photometric redshift estimates, cluster member galaxies may be included in the source catalog and therefore are incorrectly included when making the weak-lensing measurements. These galaxies are not sheared by their host cluster halo and therefore contaminate the lensing signal by diluting it. Paulus (2021) and Bocquet et al. (2023) study the impact of cluster member contamination by decomposing the source redshift distribution, $P(z)$, into uncontaminated components and contaminated components. The full model is given by the equation

$$\begin{aligned} A(R, z, \lambda) = \Sigma_{\text{NFW}}(R, r_s) / \Sigma_{\text{NFW}}(1 \text{ Mpc}/h, r_s) \\ \times \exp \left(A_\infty + \sum_i A_i \exp \left(-\frac{1}{2} \frac{(z - z_i)^2}{\rho_{\text{corr}}^2} \right) \right) \\ \times (\lambda/60)^{B_{f_{\text{cl}}}}, \quad (43) \end{aligned}$$

with the array of redshifts

$$z_i \in \{0.2, 0.28, 0.36, 0.44, 0.52, 0.6, 0.68, 0.76, 0.84, 0.92, 1\}, \quad (44)$$

where A_i , A_∞ , ρ_{corr} and $B_{f_{\text{cl}}}$ are free parameters. The fractional cluster member contamination then is

$$f_{\text{cl}}(R, z, \lambda) = A(R, z, \lambda) / (1 + A(R, z, \lambda)). \quad (45)$$

They model contaminants using the NFW profile as a fitting function with the concentration c_λ as a free parameter, defining the NFW scale radius as a function of lambda as

$$r_s = \frac{(\lambda/60)^{1/3}}{10^{c_\lambda}}. \quad (46)$$

Instead of marginalizing over the mis-centering radii distribution, we approximately account for mis-centering by simply calculating the model at the mean of the distribution. Since, for a given Rayleigh distribution $\text{Rayl}(r, \sigma_0)$, the mean is simply given by $\sigma_0 \sqrt{\pi/2}$, the mis-centering radius can be written as the mean of Eq. 42

$$R_{\text{mis}} = \sqrt{\frac{\pi}{2}} (\rho \sigma_0 + (1 - \rho) \sigma_1), \quad (47)$$

and the profiles remain constant within this radius. We model the redshift distribution of source galaxies (with source redshift z_s) as the weighted sum of the field distribution and a cluster member component, which is modeled as a Gaussian distribution of width σ_z that is offset from the cluster redshift by z_{off} :

$$\begin{aligned} P_{\text{model}}(z_s) = f_{\text{cl}} \mathcal{N}(z_s - (z_{\text{cluster}} + z_{\text{off}}), \sigma_z^2) \\ + (1 - f_{\text{cl}}) P_{\text{field}}(z_s) \\ z_{\text{off}}(z) = z_{\text{off},0} + (z_{\text{cluster}} - 0.5) z_{\text{off},1} \\ \sigma_z(z) = \sigma_{z,0} + (z_{\text{cluster}} - 0.5) \sigma_{z,1}. \quad (48) \end{aligned}$$

For each cluster, the likelihood that the observed sources are in a given radius and source redshift bin is

$$\ln \mathcal{L}_{\text{cluster}} = \sum_i w_i \ln [P_{\text{model}}(R_i, z_{s,i})] + \text{const}. \quad (49)$$

where w_i are the lensing weights of the source galaxies.

Deviating from Bocquet et al. (2023) work, we perform the analysis separately for each tomographic redshift bin. The parameter constraints for each tomographic redshift bin are given in Table B.1.

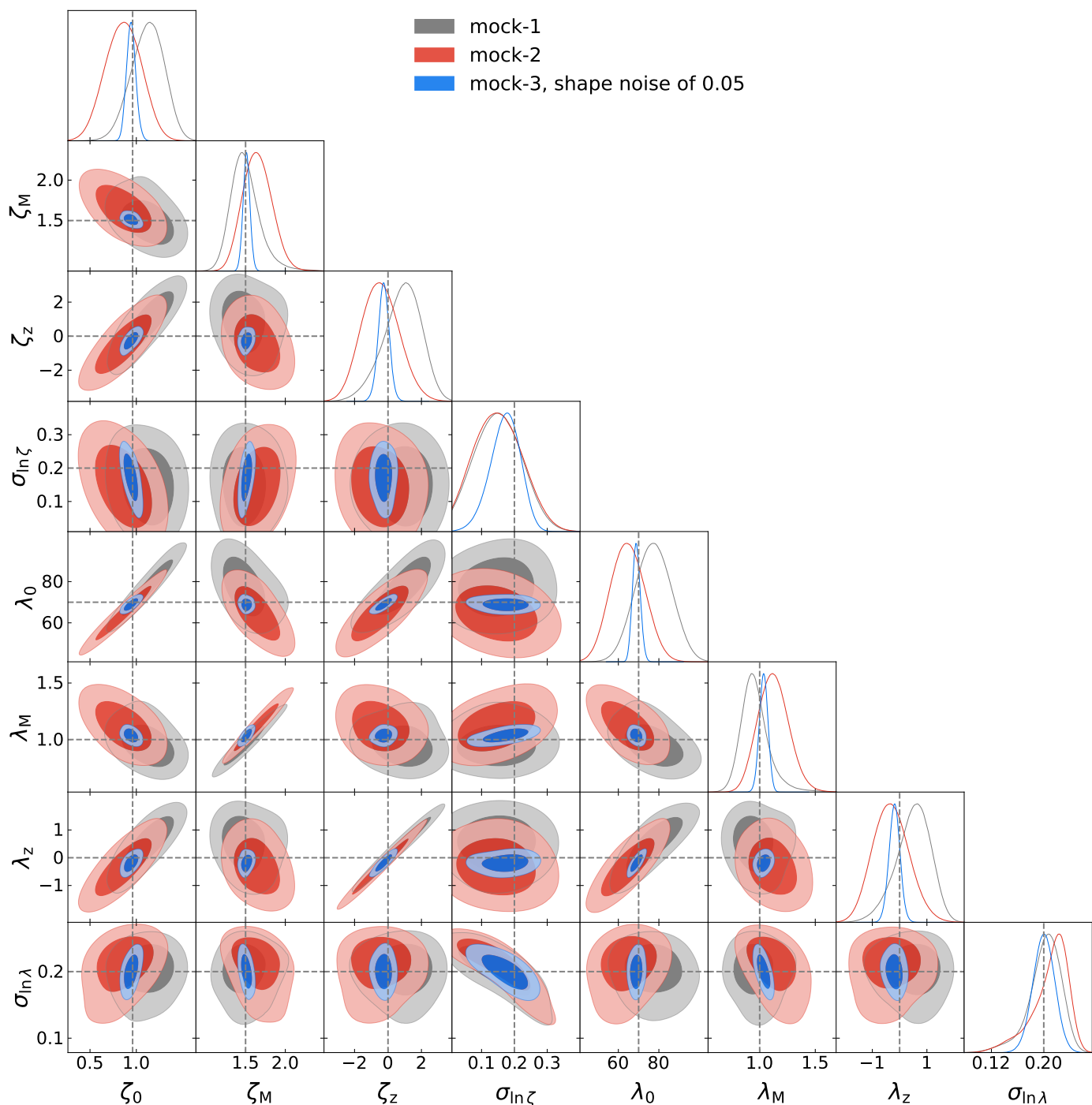


Fig. 6. Contour plot showing the posterior constraints for average cluster mass calibration of three different mock SPT samples in a fiducial flat Λ CDM cosmology. The grey dashed line shows the input parameters used to generate the mock samples, which are recovered within the uncertainties.

5. Results and discussion

In this section, we first present the tests of our new calibration method applied to the mock data in Section 5.1, and in Section 5.2 we show the resulting constraints from the real data, discuss the choices made in this analysis, such as which systematics are included, and present validation plots. We present the average cluster profile out to larger radii and compare it with the simulation in Section 5.3. In Section 5.4 we compare our results with recent literature.

5.1. Mock analysis

We validate our analysis method using a realistic SPT mock catalog with DES-like weak lensing data. For this purpose, we create mock clusters and lensing data following the approach taken in the recent SPT \times DES analysis (Bocquet et al. 2023).

We create mock SPT cluster catalogs within a fiducial cosmological model using the Tinker et al. (2008) halo mass function scaled by the surveyed volume as a function of redshift to calculate the expected number of halos as a function of redshift and mass. We impose a mass range $10^{13}M_{\odot} < M_{200c} < 10^{16}M_{\odot}$ and a redshift range $0.25 < z < 0.94$. We draw a Poisson realization of

Table 1. Cosmology and scaling-relation parameter priors in our modeling

Parameter	Units	Prior
DES Y3 cluster lensing		
$\ln M_{\text{WL}0}$	mean of bias	0
$\sigma_{\ln M_{\text{WL}0,1}}$	scaling of bias	$\mathcal{N}(0, 1)$
$\sigma_{\ln M_{\text{WL}0,2}}$	scaling of bias	$\mathcal{N}(0, 1)$
$M_{\text{WL}M}$	mass trend of bias	$\mathcal{N}(1.0, 0.006^2)$
$\ln \sigma_{\ln \text{WL}0}^2$	scaling of scatter	$\mathcal{N}(0, 1)$
$\sigma_{\ln \text{WL}M}^2$	mass trend of scatter	$\mathcal{N}(-0.226, 0.040^2)$
Cosmology		
Ω_m	-	$\mathcal{N}(0.315, 0.007)$
$\log_{10} A_s$	-	Fixed to -8.696
H_0	$\frac{\text{km}}{\text{Mpc}}$	Fixed to 70
$\Omega_{b,0}$	-	Fixed to 0.0448
n_s	-	Fixed to 0.96
w_0	-	Fixed to -1
w_a	-	Fixed to 0
$\sum m_\nu$	eV	0.06
$\Omega_{k,0}$	-	Fixed to 0
tSZE detection significance ζ -mass relation		
ζ_0	-	$\mathcal{U}(0.01, 1.5)$
ζ_M	-	$\mathcal{U}(0.5, 3)$
ζ_z	-	$\mathcal{U}(-5, 5)$
$\sigma_{\ln \zeta}$	-	$\mathcal{U}(0.01, 0.5)$
Optical richness λ -mass relation		
λ_0	-	$\mathcal{U}(10, 70)$
λ_M	-	$\mathcal{U}(0.2, 2)$
λ_z	-	$\mathcal{U}(-5, 5)$
$\sigma_{\ln \lambda}$	-	$\mathcal{U}(0.01, 0.5)$

this sample, and then for each halo we assign cluster observables (using the observable-mass relations presented in Section 4.1) and then apply survey selection cuts in tSZE detection significance ζ and richness λ consistent with those used to produce the real sample. These realistic mocks also follow the SPT survey depth geometry.

To generate mock weak lensing data for each tSZE cluster in our mock catalog, we first estimate the total source galaxies associated with the cluster by calculating its area on the sky (corresponding to the radial distance to cluster center $R = 10h^{-1}\text{Mpc}$) and assuming a source galaxy density of 6 arcmin^{-2} . We assume the same source redshift distribution as the DES-Y3 data for each tomographic bin for the mock source galaxies. For each source, we assign a weight by randomly drawing source weights from real DES data. We divide the total source galaxies equally among the three tomographic bins. We then assign distance to each source galaxy by randomly drawing distance $\propto R$. Next, for a source galaxy with distance R_i , we rescale R_i with the corresponding R_{200c} and then calculate its $\widetilde{\Delta\Sigma}$ signal using our matter profile model (see Section 4.2). In addition, we add tomographic bin-dependent cluster member contamination, consistent

with the recent measurement in DES data. Finally, we convert $\widetilde{\Delta\Sigma}$ to g_t by applying the reverse scaling. We apply scatter to each g_t measurement by drawing g_t from a normal distribution with $\sigma_{\text{eff}} = 0.3$ (effective shape noise for DES data). This process produces realistically noisy and biased tangential shear data for each cluster. Specifically, these shear data include all the known systematic and stochastic effects needed to model cluster shear profiles in DES data.

We create several independent mock catalogs to assess the performance of our likelihood model and the software. For the analysis, we divide our data into $3 \times 3 \times 3 \zeta - \lambda - z$ observable bins, and the likelihood calculation is performed following the formalism outlined in Section 4.3. Fig. 6 shows the posteriors for three mock catalogs with the same set of input scaling relations and cosmological parameters but with different uniform random deviate seed values. All the mock catalogs contain a similar number of clusters as the real SPT sample. The corresponding lensing data for mock-1 and mock-2 are generated with a shape noise ($\sigma_{\text{eff}} = 0.3$) similar to DES-Y3 lensing. The lensing data for mock-3 is created with a shape noise value of 0.05, which is equivalent to scaling up the lensing source galaxy sample by a factor of six and therefore serves as a stringent test of the software.

To effectively and efficiently sample the high dimensional parameter space, we use MULTINEST (Feroz et al. 2009, 2019) for our likelihood analysis. As is clear in Fig. 6, the posteriors show very good agreement with the input parameters (plotted as dashed lines) and show no signs of biases.

Our $\widetilde{\Delta\Sigma}$ profile analyses of both mock and real datasets typically converge in a factor of 5 less time on similar computing resources than in the case of the cluster-by-cluster analysis. Interestingly, the time required for a single iteration of the $\widetilde{\Delta\Sigma}$ likelihood is similar to that for the cluster-by-cluster analysis, but the number of iterations required for convergence is typically five times less. This faster convergence seems to be due to the difference in SNR of the average profiles as compared to the individual cluster profiles, which influences the stability of the likelihood far away from the best fit parameter values. In future analyses using the average profile method, we plan to present further efficiency improvements. Ongoing testing indicates that these approximate methods reduce the time required for a single likelihood evaluation by more than an order of magnitude.

5.2. SPT \times DES analysis

With the validation of the code, we move on to apply the analysis method outlined above to the SPT \times DES sample. Following Grandis et al. (2021), we restrict our analysis to the radial range $0.5 < R/(h^{-1}\text{Mpc}) < 3.2/(1 + z_{\text{cl}})$. This radial cut allows us to restrict the analysis to the 1-halo region while simultaneously avoiding the central region of the cluster, which is most affected by cluster member contamination, mis-centering, and baryonic processes. Throughout the analysis, we use DNF redshifts (De Vicente et al. 2016), which are used to calibrate cluster member contamination. The shape noise per tomographic bin for the DES-Y3 data is taken from Amon et al. (2022), which is in good agreement with our bootstrap error estimates

$$\sigma_{\text{eff},b} = \begin{cases} 0.243 & b = 1 \\ 0.262 & b = 2 \\ 0.259 & b = 3 \\ 0.301 & b = 4. \end{cases}$$

We analyze the SPT clusters in the redshift range $0.25 \leq z <$

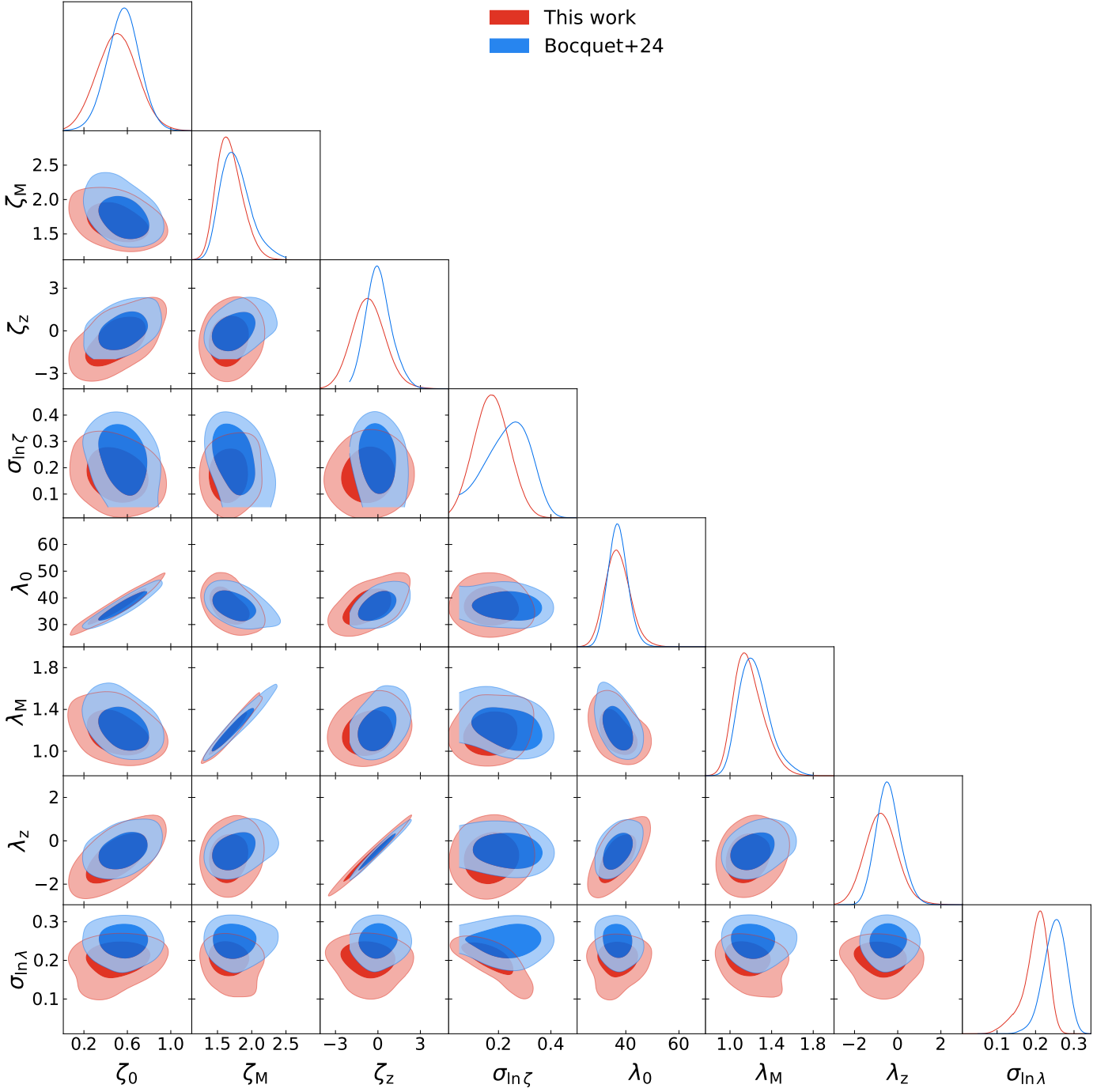


Fig. 7. Contour plot showing the posterior constraints for cluster mass calibration using average matter profiles (in red) of the SPT cluster sample in a Λ CDM model. The blue contour shows cluster-by-cluster WL-only mass calibration results from Bocquet et al. (2024) for the same SPT sample.

0.94, which contains 698 clusters with DES weak lensing data. As with the mock validation, we divide the data into $3 \times 3 \times 3$ $\hat{\zeta} - \hat{\lambda} - z$ bins, leading to 27 independent rescaled average matter $\Delta\Sigma$ profiles. Because the weak lensing signal in our sample has a higher SNR for lower redshift clusters, therefore, the highest redshift bin is chosen to be wider so that it has a sufficient SNR to approximately balance the SNR in the two lower redshift bins. Each redshift bin is further divided into 9 bins (3×3 $\hat{\zeta} - \hat{\lambda}$). Here, also, we choose bin boundary values such that each bin has a roughly similar SNR. The bin division for each redshift bin is as

follows

$$\begin{aligned} & 0.25 \leq z < 0.33 \\ & 0 \leq \hat{\lambda} < 60, 60 \leq \hat{\lambda} < 120, 120 \leq \hat{\lambda} < 250 \\ & 4.25 \leq \zeta < 5, 5 \leq \hat{\zeta} < 7, 7 \leq \hat{\zeta} < 50 \end{aligned}$$

$$\begin{aligned} & 0.33 \leq z < 0.43 \\ & 0 \leq \hat{\lambda} < 75, 75 \leq \hat{\lambda} < 120, 120 \leq \hat{\lambda} < 250 \\ & 4.25 \leq \hat{\zeta} < 6.5, 6.5 \leq \hat{\zeta} < 8.5, 8.5 \leq \hat{\zeta} < 50 \end{aligned}$$

$$\begin{aligned} & 0.43 \leq z < 0.94 \\ & 0 \leq \hat{\lambda} < 65, 65 \leq \hat{\lambda} < 110, 110 \leq \hat{\lambda} < 250 \\ & 4.25 \leq \hat{\zeta} < 5, 5 \leq \hat{\zeta} < 7, 7 \leq \hat{\zeta} < 50. \end{aligned} \tag{50}$$

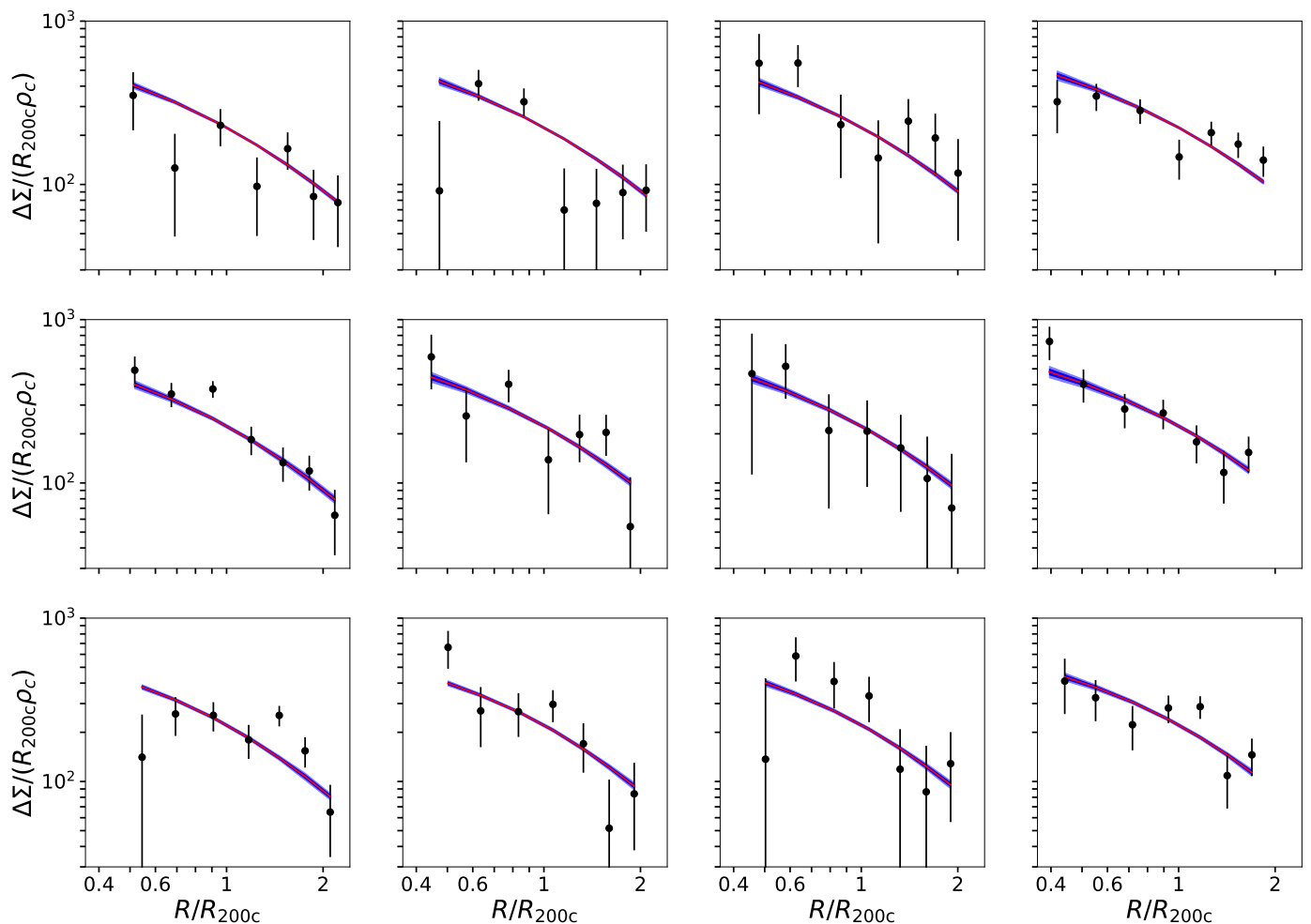


Fig. 8. Average SPT cluster profiles corresponding to the mean recovered parameters in twelve $\hat{\zeta} - \hat{\lambda} - z$ bins are shown with black data points with 1σ error bars. The weak lensing model is shown in the red line and the shaded blue region represents 2σ error region on the model.

Parameter priors for our run are listed in Table 1. In summary, we fix the sum of neutrino mass to the minimum allowed value of 0.06 eV. All other cosmological parameters are fixed to their mean Planck values (Planck Collaboration et al. 2016), except for Ω_m , which has a Gaussian prior (our results are unaffected when using a flat prior on Ω_m). The scaling relation parameters are assigned a wide flat prior. We adopt the priors on the $M_{\text{WL}} - M_{200c}$ relation parameters from Bocquet et al. (2023) where they analyze the same SPT×DES sample. Note that we follow the redshift variation of the $M_{\text{WL}} - M_{200c}$ relation by interpolating between the relations determined at specific simulation output redshifts (exactly as in Bocquet et al. 2023) rather than refitting to the functional form of the redshift dependence presented in Eqns 27 and 28. We set the mean of bias and mass trend of the bias to 0 and 1, respectively, as our model correctly accounts for redshift dependence and we observe a very high degree of self-similarity with mass.

The resulting posteriors inferred from applying the new mass calibration software to the SPT×DES data are shown in Fig. 7. The posterior mean, along with their corresponding 1σ uncertainties are shown in Table 2. We find that the mass trend ζ_M of the ζ -mass relation has a value of 1.79, which is close to the 5/3 scaling one would expect for the tSZE measured within the cluster virial region (e.g., $r < r_{200c}$). However, given the angular filtering carried out for noise reduction in SPT cluster finding, this value is likely steeper than self-similar. The redshift trend

Table 2. Mean parameter posteriors and 1σ uncertainties from our mass calibration analysis

Parameter	Posterior
tSZE detection significance ζ -mass relation	
$\ln \zeta_0$	0.586 ± 0.158
ζ_M	1.79 ± 0.195
ζ_z	0.0450 ± 1.05
$\sigma_{\ln \zeta}$	0.127 ± 0.0683
Optical richness λ -mass relation	
λ_0	37.6 ± 4.37
λ_M	1.27 ± 0.150
λ_z	-0.349 ± 0.690
$\sigma_{\ln \lambda}$	0.216 ± 0.0251

ζ_z is consistent with 0. We find that the redshift trend λ_z of the λ -mass scaling relation and the mass trend λ_M , are statistically consistent with 0 and 1 respectively.

We note that we marginalize all the crucial systematic errors in our analysis by adopting the $M_{\text{WL}} - M_{200c}$ relation. In addition, we repeat the analysis without marginalizing over the systematics and we do not notice any significant difference with or without

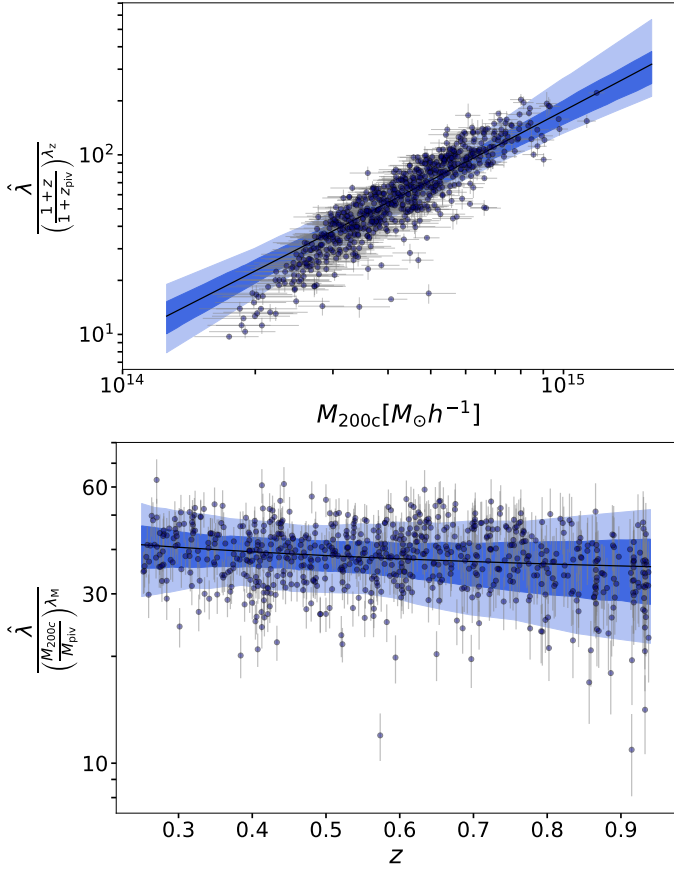


Fig. 9. The observed optical richness $\hat{\lambda}$ of SPT clusters as a function of the cluster halo mass (top) and redshift (bottom). The clusters are shown with filled circles, where the error bars capture the error in the scaling relations and the estimated cluster halo mass. The top and bottom plots shows the richness $\hat{\lambda}$ normalized at the pivot redshift $z_{\text{piv}} = 0.6$ and the pivot mass $M_{\text{piv}} = 3 \times 10^{14} h^{-1} \text{Mpc}$, respectively. The intrinsic model (Eq. 26) is shown in blue. The light and dark-shaded regions in both the panels represent 68% and 95% credibility intervals of the best-fit model respectively.

the inclusion of systematic errors in our analysis as the current error is shape noise-dominated. Bocquet et al. (2024) also find the same as shown in their Fig. 3.

5.2.1. Goodness of fit

To assess the goodness of fit of our mass calibration, we compare the average matter profile model to the average cluster profile in $3 \times 2 \times 2 \hat{\zeta} - \hat{\lambda} - z$ bins and perform a χ^2 fit to all bins. Fig. 8 shows 12 average matter profiles (represented with black data points), each for a given $\hat{\zeta} - \hat{\lambda} - z$ bin along with the model and its corresponding 2σ region (shown in shaded blue region). The profiles are extracted corresponding to the mean parameter obtained from our posterior. We obtain a $\chi^2 = 97.83$ with 84 data points from which we effectively constrain 8 parameters and this corresponds to a $\chi^2_{\text{red}} = 1.27$.

5.2.2. Scaling-relation validation tests

To further validate our mass calibration results, we perform a series of tests on the richness and tSZE scaling relations. In Fig. 9 we show $\hat{\lambda}$ -mass (top plot) and $\hat{\lambda}$ -redshift relation (bottom plot). To analyze the $\hat{\lambda}$ -mass relation, we calculate the richnesses

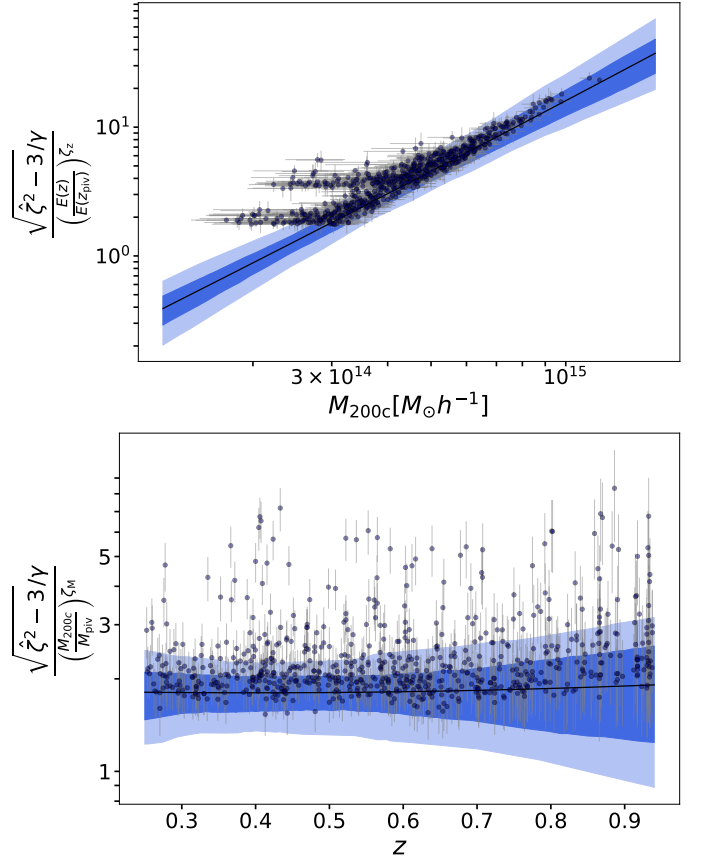


Fig. 10. The observed debiased detection significance $\hat{\zeta}$ of SPT clusters as a function of the cluster halo mass (top) and redshift (bottom). The intrinsic model (Eq. 23) is shown in blue. The plotting scheme is the same as Fig. 9. The effects of Eddington bias and selection on $\hat{\zeta}$ can be seen in the above plots.

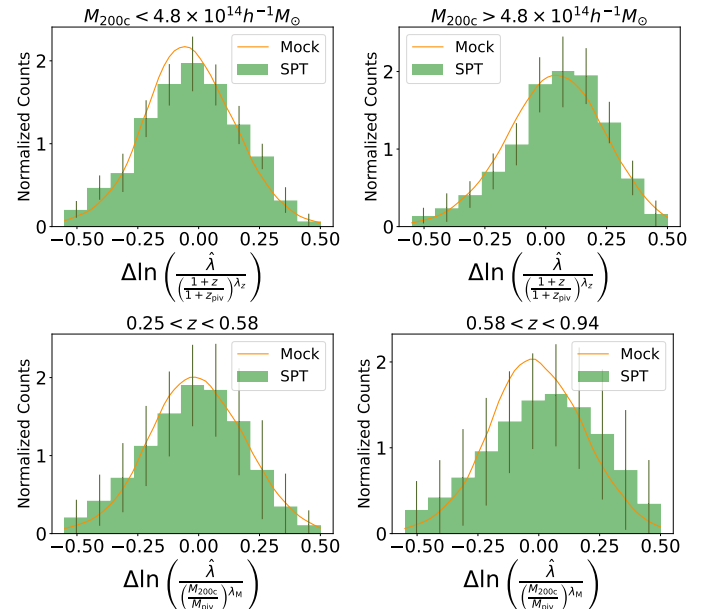


Fig. 11. Difference in normalized $\hat{\lambda}$ between the SPT sample and the best-fit intrinsic scaling relation model (x-axis) projected along the halo mass (top), analyzed in two mass bins, and projected along the redshift (bottom), analyzed in two redshift bins. The error on the histogram shows the error in the scaling relation and the Poisson noise due to binning. For comparison, the orange line shows the the same distribution for a mock sample (100 times larger than SPT sample) created using the mean scaling relation parameters obtained from the SPT analysis.

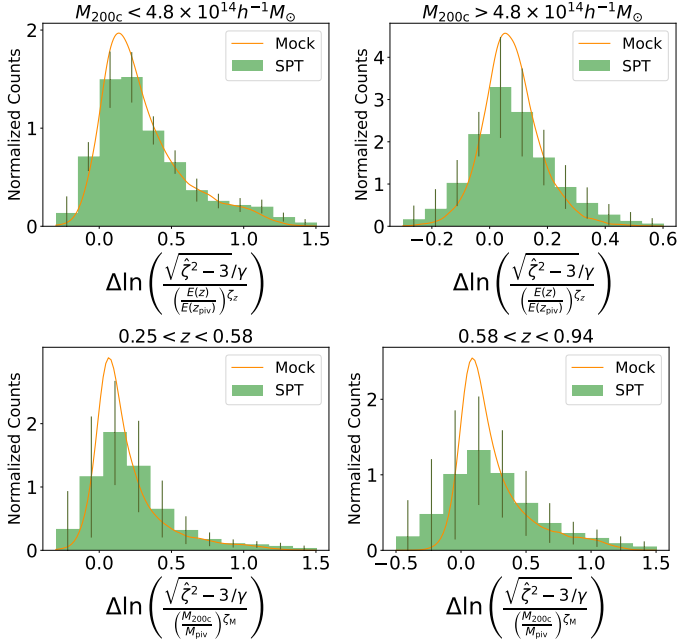


Fig. 12. Same as Fig. 11 but for normalized $\hat{\zeta}$ projected along the cluster halo mass (top), analyzed in two mass bins and projected along the redshift (bottom), analyzed in two redshift bins.

at the pivot redshift by simply dividing $\hat{\lambda}$ by $\left(\frac{1+z}{1+z_{\text{piv}}}\right)^{\lambda_z}$. This factor removes any redshift trends and allows us to study only the mass trends. On the x-axis, we show mean mass posteriors obtained using dual-observables, given by the following equation

$$P(M_{200c} | \hat{\zeta}, \hat{\lambda}, z, \mathbf{p}) = \frac{\iint d\lambda d\zeta P(\hat{\lambda} | \lambda) P(\hat{\zeta} | \zeta) P(\zeta, \lambda | M_{200c}, z, \mathbf{p}) P(M_{200c} | z, \mathbf{p})}{\iiint dM d\lambda d\zeta P(\hat{\lambda} | \lambda) P(\hat{\zeta} | \zeta) P(\zeta, \lambda | M_{200c}, z, \mathbf{p}) P(M_{200c} | z, \mathbf{p})} \quad (51)$$

Similarly, in order to study the richness-redshift relation we normalize the richnesses with $\left(\frac{M_{200c}}{M_{\text{piv}}}\right)^{\lambda_M}$. The solid black line shows the intrinsic scaling relation (Eq. 26) corresponding to the mean posterior values. The dark and light-shaded bands represent 1σ and 2σ error regions on the intrinsic scaling relation model. The grey line on the data points shows the marginalized uncertainties.

In Fig. 10 we show $\hat{\zeta}$ -mass and $\hat{\zeta}$ -redshift relation. On the y-axis, we plot $\sqrt{\hat{\zeta}^2 - 3/\gamma}$, where γ is a scaling factor that is used to correct for the different depths of fields in the SPT survey. Again, we normalize the y-axis with a factor of $\left(\frac{E(z)}{E(z_{\text{piv}})}\right)^{\zeta_z}$ while analyzing the relation with mass and with a factor of $\left(\frac{M_{200c}}{M_{\text{piv}}}\right)^{\zeta_M}$ while analyzing its relation with redshift. The best-fit intrinsic scaling relation model (Eq. 23) is shown with a black line and the error region is shown in blue bands.

Compared to the intrinsic scaling relation (blue bands) the observables in our analysis suffer from selection cuts and Eddington bias which can be seen in Fig. 9 & 10. The Eddington bias is clearly visible in the lower-left corner of the top plot (Fig. 10) from the points lying above the best-fitting line, i.e. they are preferentially scattered towards higher observable $\hat{\zeta}$. To understand whether the data points are behaving consistently with expectation, we create a mock sample 100 times larger than SPT sample using the mean values from the parameter posteriors and

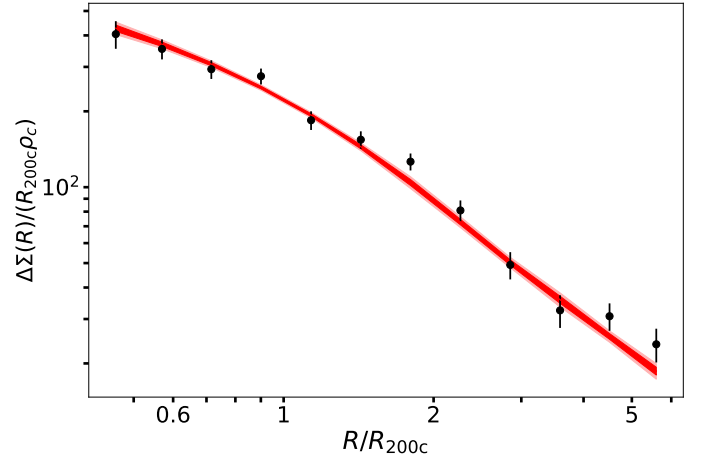


Fig. 13. Average matter profile over the full mass and redshift ranges estimated using the mean mass from our posteriors compared to the WL model at the mean redshift. The black points represent the measured mean profile, and the error bars include not only shape noise but also the impact of the mass uncertainties. The dark and light-shaded red bands show 1σ and 2σ error regions, respectively, on the model extracted from hydrodynamical simulations.

apply the same selection cut as was applied to the real data. The comparison of the mock and the real data then allows for robust validation.

In Fig. 11 we plot the difference between the normalized $\hat{\lambda}$ and the best-fit intrinsic scaling relation model in log space, projected along the mass in different mass bins (top plot) and different redshift bins (bottom plot). We perform the above analysis for the real data and the mock sample and compare the two to validate consistency with our richness scatter model.

The orange line represents mocks and the green histogram is the SPT sample. The green line represents the error bar due to uncertainties in the scaling relation parameters and the Poisson error that arises from the binning. We see a good agreement between the mock and the SPT sample in mass and redshift bins suggesting that our scatter model is capable of reproducing the data within one standard deviation.

Similarly, in Fig. 12 we show the difference between the normalized $\hat{\zeta}$ and the best-fit intrinsic scaling relation model in the x-axis and the normalized counts in the y-axis for the SPT sample and the mock sample. Our data shows good agreement with the mock in two mass (top plot) and two redshift bins (bottom plot) and suggests no trends with mass or redshift. The shift in the histogram peak away from zero is reflective of Eddington bias and $\hat{\zeta}$ selection which is more pronounced when compared to richness.

5.3. Mass profile extending to cluster outskirts

In our mass calibration analysis, we restricted our radial range to $R < 3.2/(1+z)h^{-1}\text{Mpc}$ to avoid contribution from the 2-halo regime. Using our mass calibration results (Table 2), we combine the whole SPT sample with redshift, $0.25 < z < 0.94$ and all masses to create an average rescaled matter profile $\Delta \Sigma$ including regions beyond the 1-halo. We create 200 realizations of the average matter profile using the posterior values to marginalize over the observable-mass relation parameter uncertainty in the profile. SNR of the full average matter profile is ~ 36 out to $6 R/R_{200c}$. Fig. 13 shows the full profile compared to the mean model calculated at the mean redshift of the sample. The light and dark-shaded red bands represent the 1σ and 2σ error re-

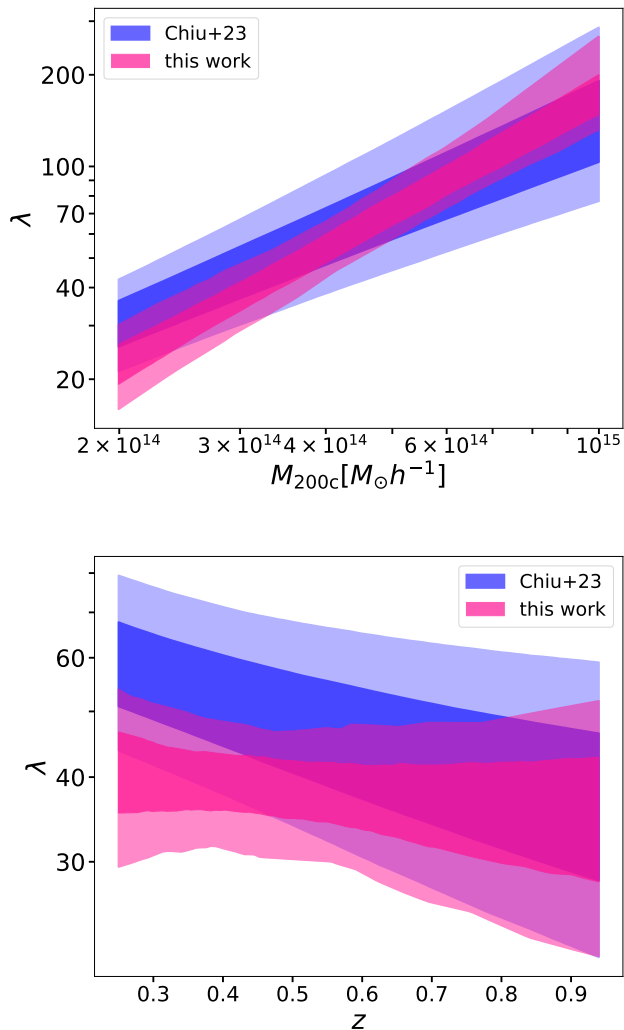


Fig. 14. Best fit $\lambda - M$ (top) and $\lambda - z$ (bottom) models evaluated at our pivot mass and redshift, compared to Chiu et al. (2023) work (in blue). Dark and light-shaded regions represent 1σ and 2σ regions respectively. Our work (in pink) shows very good agreement with the blue model.

regions respectively. We obtain a $\chi^2_{\text{red}} = 1.15$, which suggests that the model and data are in good agreement even in the cluster outskirts.

5.4. Comparison to previous work

In this section, we compare our tSZE and richness scaling relation results to previous studies. Chiu et al. (2023) analyzed eROSITA Final Equatorial Depth Survey (eFEDS) clusters with Hyper Suprime-Cam (HSC) weak lensing data along with MCMF richness and calibrated richness-mass-redshift relation. Their results are shown in shaded blue color in Fig. 14 plotted at our pivot redshift of 0.6 and pivot mass of $M_{200c} = 3 \times 10^{14} h^{-1} \text{Mpc}$. Since their analysis is performed with M_{500c} , we use the conversion relation mentioned in Ragagnin et al. (2020) to convert M_{500c} to M_{200c} . Our work (in pink) results in tighter constraints than Chiu et al. (2023) and is in good agreement with their work. The blue contours in Fig. 7 show the constraints from Bocquet et al. (2024) weak lensing analysis of the same SPT×DES sample with MCMF center and DNF redshifts. They perform the analysis on a cluster-by-cluster basis compared to our average profile approach

and they use the same radial fitting range as ours. Our analysis is done with a prior on Ω_m unlike in Bocquet et al. (2024), where they use a flat prior. We use a wider prior on $\sigma_{\ln \zeta}$ and ζ_z compared to their work as can be seen in Fig. 7. The results from our analysis show very good agreement with their single cluster analysis method and every parameter agrees on average at $\approx 0.4\sigma$ level.

6. Summary

In this work, we study galaxy cluster profiles in *Magneticum* and Illustris-TNG simulations and find remarkable self-similarity among galaxy clusters with varying redshift and masses. In particular, we analyze the scaled differential surface mass density ($\Delta\Sigma/(R_{200c}\rho_{\text{crit}})$) as a function of the scaled radius (R/R_{200c}). Rescaling individual profiles by their corresponding R_{200c} and associated critical density ($\rho_{\text{crit}}(z)$) significantly reduces the mass and redshift dependence respectively. We quantify the observed self-similarity by computing fractional scatter with redshift and mass in the rescaled space and compare it with the fractional scatter obtained in physical space. The fractional scatter with redshift is roughly 6 times lower in rescaled space. We see a remarkably low fractional scatter with mass in rescaled space of $\approx 1\%$ which is ≈ 23 times lower than the fractional scatter obtained in physical space. This self-similar behavior is ideal for analyzing the average cluster profiles, because it minimizes the cluster-to-cluster variation among the profiles and allows one to combine clusters with a wide range of redshift and mass, enabling studies cluster matter profiles in a high SNR regime.

We exploit the self-similarity of the average matter profiles in the rescaled space to calibrate the masses of SPT tSZE-selected clusters. For this, we construct the lensing model using the simulations accounting for small redshift trends and assuming perfect self-similarity with mass. We create average SPT × DES-WL cluster profiles with their appropriate weights and account for all crucial systematic errors through the $M_{\text{WL}} - M_{200c}$ relation. Our likelihood constrains the $\lambda - M - z$ and $\zeta - M - z$ relation parameters and takes into account the observational and intrinsic scatter on the observables. Additionally, we account for the Eddington and Malmquist biases that arise from the selection applied to the observables in defining the cluster sample.

We calibrate the $\lambda - M - z$ and $\zeta - M - z$ scaling relations using the average mass profile calibration method described in this paper and simultaneously constrain the amplitude, the mass trend, the redshift trend, and the intrinsic scatter for both scaling relations. Our findings for the mass trend are consistent with the self-similar expectations for both richness and zeta scaling relations. We find a negative value for the redshift trend in richness, $\lambda_z = -0.349 \pm 0.690$, and tSZE ζ , $\zeta_z = 0.045 \pm 1.05$, which is consistent with zero in both cases. Our constraints on $\lambda - M - z$ parameters appear to be in good agreement with Chiu et al. (2023) who analyzed the eFEDS clusters with HSC weak lensing. Bocquet et al. (2024) analyze the same SPT-cl sample with DES-WL on a cluster-by-cluster basis; our results from the average matter profile analysis for both the scaling relations are in good agreement with their work. Furthermore, we find that our SPT×DES average matter profile of 698 clusters out to $6R/R_{200c}$ shows good agreement with a Λ CDM model.

The upcoming stage IV weak-lensing surveys will offer us a vast amount of much higher quality lensing data. The average profile mass calibration method, which we have successfully demonstrated here is an ideal way of analyzing the future datasets, and it will enable efficient analyses of much larger cluster samples for cosmology and structure formation constraints. Analyzing av-

erage cluster matter profiles in rescaled space will further help us create high SNR profiles by combining cluster measurements over wide redshift and mass ranges. The shape of the average cluster matter profile can then be used to study baryonic feedback, different modified gravity models, and the collisional nature of dark matter.

Acknowledgements

We acknowledge financial support from the MPG Faculty Fellowship program and the Ludwig-Maximilians-Universität (LMU-Munich).

The South Pole Telescope program is supported by the National Science Foundation (NSF) through the Grant No. OPP-1852617. Partial support is also provided by the Kavli Institute of Cosmological Physics at the University of Chicago. PISCO observations were supported by US NSF grant AST-0126090. Work at Argonne National Laboratory was supported by the U.S. Department of Energy, Office of High Energy Physics, under Contract No. DE-AC02-06CH11357.

Funding for the DES Projects has been provided by the U.S. Department of Energy, the U.S. National Science Foundation, the Ministry of Science and Education of Spain, the Science and Technology Facilities Council of the United Kingdom, the Higher Education Funding Council for England, the National Center for Supercomputing Applications at the University of Illinois at Urbana-Champaign, the Kavli Institute of Cosmological Physics at the University of Chicago, the Center for Cosmology and Astro-Particle Physics at the Ohio State University, the Mitchell Institute for Fundamental Physics and Astronomy at Texas A&M University, Financiadora de Estudos e Projetos, Fundação Carlos Chagas Filho de Amparo à Pesquisa do Estado do Rio de Janeiro, Conselho Nacional de Desenvolvimento Científico e Tecnológico and the Ministério da Ciência, Tecnologia e Inovação, the Deutsche Forschungsgemeinschaft and the Collaborating Institutions in the Dark Energy Survey.

The Collaborating Institutions are Argonne National Laboratory, the University of California at Santa Cruz, the University of Cambridge, Centro de Investigaciones Energéticas, Medioambientales y Tecnológicas-Madrid, the University of Chicago, University College London, the DES-Brazil Consortium, the University of Edinburgh, the Eidgenössische Technische Hochschule (ETH) Zürich, Fermi National Accelerator Laboratory, the University of Illinois at Urbana-Champaign, the Institut de Ciències de l'Espai (IEEC/CSIC), the Institut de Física d'Altes Energies, Lawrence Berkeley National Laboratory, the Ludwig-Maximilians Universität München and the associated Excellence Cluster Universe, the University of Michigan, NSF's NOIRLab, the University of Nottingham, The Ohio State University, the University of Pennsylvania, the University of Portsmouth, SLAC National Accelerator Laboratory, Stanford University, the University of Sussex, Texas A&M University, and the OzDES Membership Consortium.

Based in part on observations at Cerro Tololo Inter-American Observatory at NSF's NOIRLab (NOIRLab Prop. ID 2012B-0001; PI: J. Frieman), which is managed by the Association of Universities for Research in Astronomy (AURA) under a cooperative agreement with the National Science Foundation.

The DES data management system is supported by the National Science Foundation under Grant Numbers AST-1138766 and AST-1536171. The DES participants from Spanish institutions are partially supported by MICINN under grants ESP2017-89838, PGC2018-094773, PGC2018-102021, SEV-2016-0588, SEV-2016-0597, and MDM-2015-0509, some of which include

ERDF funds from the European Union. IFAE is partially funded by the CERCA program of the Generalitat de Catalunya. Research leading to these results has received funding from the European Research Council under the European Union's Seventh Framework Program (FP7/2007-2013) including ERC grant agreements 240672, 291329, and 306478. We acknowledge support from the Brazilian Instituto Nacional de Ciência e Tecnologia (INCT) do e-Universo (CNPq grant 465376/2014-2).

This manuscript has been authored by Fermi Research Alliance, LLC under Contract No. DE-AC02-07CH11359 with the U.S. Department of Energy, Office of Science, Office of High Energy Physics.

Data Availability

The data underlying this article will be shared upon reasonable request to the corresponding author.

References

- Abbott, T. M. C., Aguena, M., Alarcon, A., et al. 2020, *Phys. Rev. D*, 102, 023509
- Abbott, T. M. C., Aguena, M., Alarcon, A., et al. 2022, *Phys. Rev. D*, 105, 023520
- Amon, A., Gruen, D., Troxel, M., et al. 2022, *Physical Review D*, 105
- Arnaud, M., Pratt, G. W., Piffaretti, R., et al. 2010, *Astronomy and Astrophysics*, 517, A92
- Baldi, A., Ettori, S., Molendi, S., & Gastaldello, F. 2012, *A&A*, 545, A41
- Bartelmann, M. 1996, *A&A*, 313, 697
- Beck, A. M., Murante, G., Arth, A., et al. 2016, *MNRAS*, 455, 2110
- Becker, M. R. & Kravtsov, A. V. 2011, *ApJ*, 740, 25
- Bellagamba, F., Sereno, M., Roncarelli, M., et al. 2019, *MNRAS*, 484, 1598
- Bhattacharya, S., Habib, S., Heitmann, K., & Vikhlinin, A. 2013, *Astrophys. J.*, 766, 32
- Bleem, L. E., Bocquet, S., Stalder, B., et al. 2020, *The Astrophysical Journal Supplement Series*, 247, 25
- Bleem, L. E., Klein, M., Abbott, T. M. C., et al. 2023, *Galaxy Clusters Discovered via the Thermal Sunyaev-Zel'dovich Effect in the 500-square-degree SPTpol Survey*
- Bleem, L. E., Stalder, B., de Haan, T., et al. 2015, *ApJS*, 216, 27
- Bocquet, S., Dietrich, J. P., Schrabback, T., et al. 2019, *The Astrophysical Journal*, 878, 55
- Bocquet, S., Grandis, S., Bleem, L. E., et al. 2023, *arXiv e-prints*, arXiv:2310.12213
- Bocquet, S., Grandis, S., Bleem, L. E., et al. 2024, *arXiv e-prints*, arXiv:2401.02075
- Bocquet, S., Saro, A., Dolag, K., & Mohr, J. J. 2016, *MNRAS*, 456, 2361
- Bulbul, E., Chiu, I. N., Mohr, J. J., et al. 2019, *ApJ*, 871, 50
- Carlstrom, J. E., Ade, P. A. R., Aird, K. A., et al. 2011, *PASP*, 123, 568
- Cataneo, M., Rapetti, D., Schmidt, F., et al. 2015, *Phys. Rev. D*, 92, 044009
- Chiu, I., Mohr, J., McDonald, M., et al. 2016, *MNRAS*, 455, 258
- Chiu, I., Mohr, J. J., McDonald, M., et al. 2018, *MNRAS*, 478, 3072
- Chiu, I. N., Klein, M., Mohr, J., & Bocquet, S. 2023, *MNRAS*, 522, 1601
- Costanzi, M., Rozo, E., Simet, M., et al. 2019, *MNRAS*, 488, 4779
- Costanzi, M., Saro, A., Bocquet, S., et al. 2021, *Phys. Rev. D*, 103, 043522
- Covone, G., Sereno, M., Kilbinger, M., & Cardone, V. F. 2014, *Astrophys. J. Lett.*, 784, L25
- De Vicente, J., Sánchez, E., & Sevilla-Noarbe, I. 2016, *MNRAS*, 459, 3078
- Dietrich, J. P., Bocquet, S., Schrabback, T., et al. 2018, *Monthly Notices of the Royal Astronomical Society*, 483, 2871
- Dietrich, J. P., Bocquet, S., Schrabback, T., et al. 2019, *MNRAS*, 483, 2871
- Dolag, K., Mevius, E., & Remus, R.-S. 2017, *Galaxies*, 5, 35
- Feroz, F., Hobson, M. P., & Bridges, M. 2009, *Monthly Notices of the Royal Astronomical Society*, 398, 1601
- Feroz, F., Hobson, M. P., Cameron, E., & Pettitt, A. N. 2019, *The Open Journal of Astrophysics*, 2
- Finoguenov, A., Reiprich, T. H., & Böhringer, H. 2001, *A&A*, 368, 749
- Flaugher, B., Diehl, H. T., Honscheid, K., et al. 2015, *AJ*, 150, 150
- Gatti, M., Giannini, G., Bernstein, G. M., et al. 2022, *MNRAS*, 510, 1223
- Gatti, M., Sheldon, E., Amon, A., et al. 2021, *MNRAS*, 504, 4312
- Ghirardini, V., Bulbul, E., Artis, E., et al. 2024, *The SRG/eROSITA All-Sky Survey: Cosmological Constraints from Cluster Abundances in the Western Galactic Hemisphere*
- Gioielli, C., Marulli, F., Moscardini, L., et al. 2021, *A&A*, 653, A19
- Grandis, S., Bocquet, S., Mohr, J. J., Klein, M., & Dolag, K. 2021, *MNRAS*, 507, 5671

- Haiman, Z., Mohr, J. J., & Holder, G. P. 2001, *ApJ*, 553, 545
- Hirschmann, M., Dolag, K., Saro, A., et al. 2014, *MNRAS*, 442, 2304
- Huff, E. & Mandelbaum, R. 2017, arXiv e-prints, arXiv:1702.02600
- Jarvis, M., Bernstein, G. M., Amon, A., et al. 2021, *MNRAS*, 501, 1282
- Kaiser, N. 1986, *MNRAS*, 222, 323
- Klein, M., Grandis, S., Mohr, J. J., et al. 2019, *MNRAS*, 488, 739
- Klein, M., Mohr, J. J., Bocquet, S., et al. 2023, arXiv e-prints, arXiv:2309.09908
- Klein, M., Mohr, J. J., Desai, S., et al. 2018, *MNRAS*, 474, 3324
- Komatsu, E., Smith, K. M., Dunkley, J., et al. 2011, *ApJS*, 192, 18
- Lau, E. T., Nagai, D., Avestruz, C., Nelson, K., & Vikhlinin, A. 2015, *The Astrophysical Journal*, 806, 68
- Lesci, G. F., Marulli, F., Moscardini, L., et al. 2022, *A&A*, 659, A88
- MacCrann, N., Becker, M. R., McCullough, J., et al. 2022, *MNRAS*, 509, 3371
- Mantz, A., Allen, S. W., Rapetti, D., & Ebeling, H. 2010, *MNRAS*, 406, 1759
- Mantz, A. B., Allen, S. W., Morris, R. G., et al. 2014, *MNRAS*, 440, 2077
- Marinacci, F., Vogelsberger, M., Pakmor, R., et al. 2018, *MNRAS*, 480, 5113
- Mazoun, A., Bocquet, S., Garny, M., et al. 2023, arXiv e-prints, arXiv:2312.17622
- McClintock, T., Varga, T., Gruen, D., et al. 2018, *Monthly Notices of the Royal Astronomical Society*, 482, 1352–1378
- McDonald, M., Benson, B. A., Vikhlinin, A., et al. 2014, *ApJ*, 794, 67
- Melin, J. B., Bartlett, J. G., & Delabrouille, J. 2006, *A&A*, 459, 341
- Mohr, J. J. & Evrard, A. E. 1997, *ApJ*, 491, 38
- Mohr, J. J., Mathiesen, B., & Evrard, A. E. 1999, *ApJ*, 517, 627
- Myles, J., Alarcon, A., Amon, A., et al. 2021, *MNRAS*, 505, 4249
- Naiman, J. P., Pillepich, A., Springel, V., et al. 2018, *MNRAS*, 477, 1206
- Navarro, J. F., Frenk, C. S., & White, S. D. M. 1996, *The Astrophysical Journal*, 462, 563
- Navarro, J. F., Frenk, C. S., & White, S. D. M. 1997, *The Astrophysical Journal*, 490, 493
- Nelson, D., Pillepich, A., Springel, V., et al. 2018, *MNRAS*, 475, 624
- Nelson, D., Springel, V., Pillepich, A., et al. 2019, *Computational Astrophysics and Cosmology*, 6, 2
- Nelson, K., Lau, E. T., & Nagai, D. 2014, *The Astrophysical Journal*, 792, 25
- Oguri, M. & Takada, M. 2011, *Phys. Rev. D*, 83, 023008
- Okabe, N., Smith, G. P., Umetsu, K., Takada, M., & Futamase, T. 2013, *The Astrophysical Journal Letters*, 769, L35
- Okabe, N., Zhang, Y.-Y., Finoguenov, A., et al. 2010, *The Astrophysical Journal*, 721, 875
- Paulus, M. 2021, PhD thesis, Ludwig-Maximilians University of Munich, Germany
- Pillepich, A., Nelson, D., Hernquist, L., et al. 2018, *MNRAS*, 475, 648
- Planck Collaboration, Ade, P. A. R., Aghanim, N., et al. 2016, *A&A*, 594, A24
- Planck Collaboration & et al. 2016, *A&A*, 594, A13
- Ragagnin, A., Saro, A., Singh, P., & Dolag, K. 2020, *Monthly Notices of the Royal Astronomical Society*, 500, 5056
- Schneider, P. 2006, *Weak Gravitational Lensing* (Springer Berlin Heidelberg), 269–451
- Severini, T. A. 2004, *Bernoulli*, 10, 421
- Sevilla-Noarbe, I., Bechtol, K., Carrasco Kind, M., et al. 2021, *ApJS*, 254, 24
- Sheldon, E. S. & Huff, E. M. 2017, *ApJ*, 841, 24
- Springel, V., Pakmor, R., Pillepich, A., et al. 2018, *MNRAS*, 475, 676
- Teklu, A. F., Remus, R.-S., Dolag, K., et al. 2015, *ApJ*, 812, 29
- Tinker, J., Kravtsov, A. V., Klypin, A., et al. 2008, *The Astrophysical Journal*, 688, 709
- To, C., Krause, E., Rozo, E., et al. 2021, *Phys. Rev. Lett.*, 126, 141301
- Umetsu, K., Medezinski, E., Nonino, M., et al. 2014, *The Astrophysical Journal*, 795, 163
- Umetsu, K., Zitrin, A., Gruen, D., et al. 2016, *Astrophys. J.*, 821, 116
- Vanderlinde, K., Crawford, T. M., de Haan, T., et al. 2010, *ApJ*, 722, 1180
- Vikhlinin, A., Kravtsov, A., Forman, W., et al. 2006, *The Astrophysical Journal*, 640, 691–709
- Vikhlinin, A., Kravtsov, A. V., Burenin, R. A., et al. 2009, *ApJ*, 692, 1060
- Vogt, S. M. L., Bocquet, S., Davies, C. T., Mohr, J. J., & Schmidt, F. 2024, arXiv e-prints, arXiv:2401.09959
- von der Linden, A., Allen, M. T., Applegate, D. E., et al. 2014, *MNRAS*, 439, 2
- White, S. D. M., Efstathiou, G., & Frenk, C. S. 1993, *MNRAS*, 262, 1023
- Zubeldia, Í. & Challinor, A. 2019, *MNRAS*, 489, 401

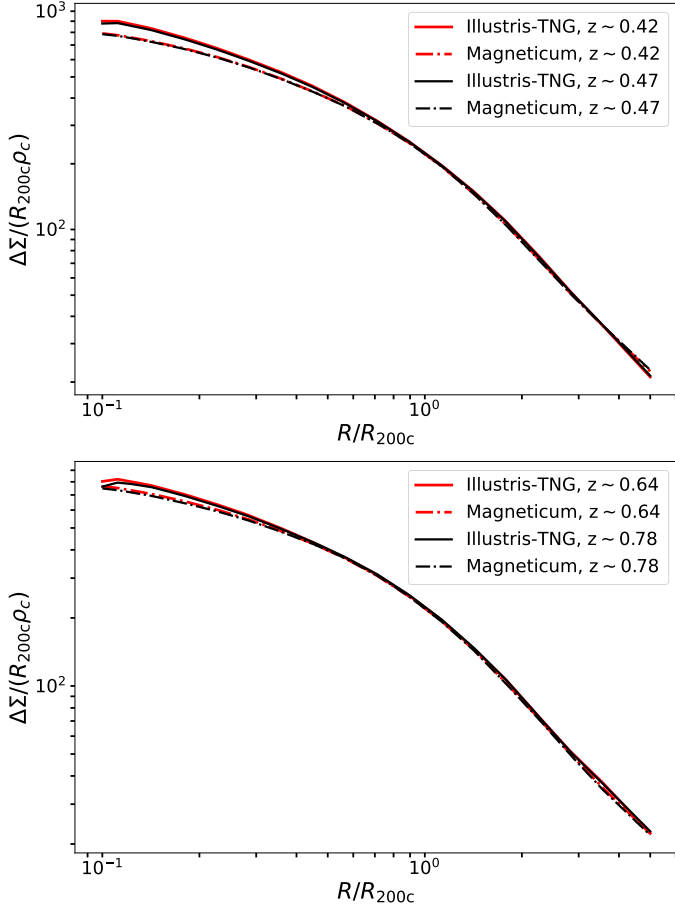


Fig. A.1. Comparison of average matter profiles from Illustris-TNG and *Magneticum* at the redshift of 0.42 and 0.47 (top figure) and at the redshift of 0.64 and 0.78 (bottom figure). The profiles exhibit very small differences with a small redshift change for a given simulation throughout the radial range.

Appendix A: Cluster Profile interpolation

In Fig. A.1 top figure, we show the differences in the Illustris-TNG average cluster profiles at 0.42 vs. 0.47 in solid red and solid black lines respectively. In dashed red and black lines we show a average cluster profile in *Magneticum* at the redshift of 0.42 and 0.47 respectively. The profiles show very small differences with slight changes in redshift. Similarly in the bottom figure, we compare the profiles at the redshift of 0.64 vs. 0.78 and find that in both simulation profiles exhibit minor differences. The purpose of this plot is not to compare the different simulations themselves, but, the differences in the simulations in the inner radial region at the same redshift are due to different baryonic effects.

Appendix B: Robustness of SPT-cl analysis

In this section, we assess the robustness of our analysis method by changing the inner fitting region of the cluster profile and also by changing the binning of the sample in $\hat{\zeta} - \hat{\lambda} - z$. In the top figure of Fig. B.1 we compare the posterior of the scaling relation parameter for inner fitting radii of $0.5h^{-1}\text{Mpc}$ and $0.7h^{-1}\text{Mpc}$ (Note that for this analysis we have binned our observables in $3 \times 3 \times 3$ bins). The blue posterior ($R > 0.7h^{-1}\text{Mpc}$) results in a larger error compared to the red posterior which is consistent with the fact that we have fewer source galaxies as we have restricted our fitting range.

In the bottom figure of Fig. B.1, we compare the scaling relation parameters posterior resulting from different binning of observables for the SPT sample compared to our fiducial $3 \times 3 \times 3$ binning. For the new binning, we divide our observables in $3 \times 2 \times 2$ bins as follows

$$\begin{aligned}
& 0.25 \leq z < 0.33 \\
& 0 \leq \hat{\lambda} < 80, 80 \leq \hat{\lambda} < 243 \\
& 4.25 \leq \hat{\zeta} < 6, 6 \leq \hat{\zeta} < 50 \\
\\
& 0.33 \leq z < 0.43 \\
& 0 \leq \hat{\lambda} < 95, 95 \leq \hat{\lambda} < 243 \\
& 4.25 \leq \hat{\zeta} < 7.5, 7.5 \leq \hat{\zeta} < 50 \\
\\
& 0.43 \leq z < 0.94 \\
& 0 \leq \hat{\lambda} < 85, 85 \leq \hat{\lambda} < 243 \\
& 4.25 \leq \hat{\zeta} < 6, 6 \leq \hat{\zeta} < 50.
\end{aligned} \tag{B.1}$$

The above binning is such that each redshift bin is further divided into roughly similar SNR. The blue and red posteriors show very good agreement with each other and the choice of binning doesn't result in a big shift in parameter values. This test ensures that our scaling parameter constraints are insensitive to the choice of $\hat{\zeta} - \hat{\lambda} - z$ bins.

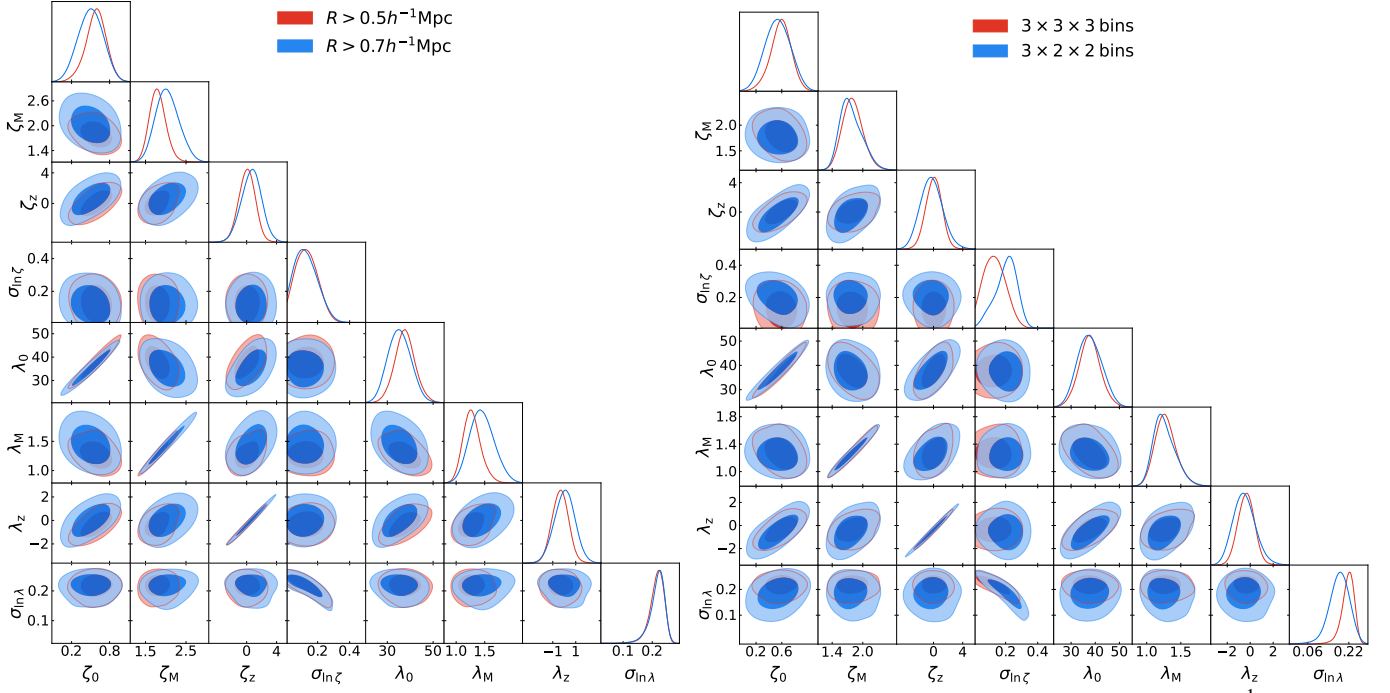


Fig. B.1. Comparison of the posterior for the SPT sample with the same binning but different inner radius fit (left figure) of $0.5h^{-1}\text{Mpc}$ (red) and $0.7h^{-1}\text{Mpc}$ (blue). The blue posterior is in good agreement with the red posterior with a slightly larger error region. In the right figure, we compare the results from two different binning while keeping the inner-fitting radii fixed at $0.5h^{-1}\text{Mpc}$. We see a good agreement between the two results suggesting our results are not heavily affected by the choice of binning.

Table B.1. Parameters of the cluster member contamination model (mean and standard deviation).

Parameter	DNF photo- z and MCMF center		
	Tomographic redshift bin 2	Tomographic redshift bin 3	Tomographic redshift bin 4
$z_{\text{off},0}$	-0.009 ± 0.002	0.05 ± 0.002	0.16 ± 0.0061
$z_{\text{off},1}$	-0.22 ± 0.020	-0.23 ± 0.017	-0.45 ± 0.022
$\sigma_{z,0}$	0.04 ± 0.002	0.07 ± 0.002	0.13 ± 0.0065
$\sigma_{z,1}$	-0.018 ± 0.021	-0.086 ± 0.017	-0.16 ± 0.019
$\log(c)$	0.44 ± 0.035	0.51 ± 0.041	0.26 ± 0.062
B_λ	0.78 ± 0.039	0.60 ± 0.042	0.53 ± 0.066
ρ_{corr}	0.27 ± 0.015	0.18 ± 0.010	0.49 ± 0.0063
A_0	0.12 ± 0.058	-0.326 ± 0.171	0.16 ± 0.028
A_1	0.19 ± 0.042	-0.220 ± 0.130	0.16 ± 0.027
A_2	0.29 ± 0.044	-0.010 ± 0.12	0.17 ± 0.026
A_3	0.42 ± 0.053	0.307 ± 0.119	0.18 ± 0.025
A_4	0.53 ± 0.059	0.640 ± 0.111	0.19 ± 0.026
A_5	0.62 ± 0.060	0.867 ± 0.114	0.19 ± 0.025
A_6	0.68 ± 0.060	0.877 ± 0.124	0.20 ± 0.025
A_7	0.72 ± 0.061	0.694 ± 0.122	0.21 ± 0.025
A_8	0.74 ± 0.071	0.441 ± 0.134	0.22 ± 0.026
A_9	0.75 ± 0.081	0.238 ± 0.168	0.22 ± 0.027
A_{10}	0.75 ± 0.096	0.133 ± 0.208	0.23 ± 0.028
A_∞	-4.9 ± 0.057	-4.61 ± 0.378	-4.76 ± 0.211

Affiliations

1. University Observatory, Faculty of Physics, Ludwig-Maximilians-Universität, Scheinerstr. 1, 81679 Munich, Germany
2. Max Planck Institute for Extraterrestrial Physics, Giessenbachstr. 1, 85748 Garching, Germany
3. Universität Innsbruck, Institut für Astro- und Teilchenphysik, Technikerstr. 25/8, 6020 Innsbruck, Austria
4. Laboratório Interinstitucional de e-Astronomia - LIneA, Rua Gal. José Cristino 77, Rio de Janeiro, RJ - 20921-400, Brazil
5. Fermi National Accelerator Laboratory, P. O. Box 500, Batavia, IL 60510, USA
6. Department of Physics, University of Michigan, Ann Arbor, MI 48109, USA
7. Instituto de Física Teórica, Universidade Estadual Paulista, São Paulo, Brazil
8. Institute of Cosmology and Gravitation, University of Portsmouth, Portsmouth, PO1 3FX, UK
9. Department of Physics and Astronomy, Pevensey Building, University of Sussex, Brighton, BN1 9QH, UK
10. Department of Physics & Astronomy, University College London, Gower Street, London, WC1E 6BT, UK
11. Instituto de Astrofísica de Canarias, E-38205 La Laguna, Tenerife, Spain
12. Institut de Física d'Altes Energies (IFAE), The Barcelona Institute of Science and Technology, Campus UAB, 08193 Bellaterra (Barcelona) Spain
13. Astronomy Unit, Department of Physics, University of Trieste, via Tiepolo 11, I-34131 Trieste, Italy
14. INAF-Osservatorio Astronomico di Trieste, via G. B. Tiepolo 11, I-34143 Trieste, Italy
15. Institute for Fundamental Physics of the Universe, Via Beirut 2, 34014 Trieste, Italy
16. Hamburger Sternwarte, Universität Hamburg, Gojenbergsweg 112, 21029 Hamburg, Germany
17. Department of Physics, IIT Hyderabad, Kandi, Telangana 502285, India
18. Jet Propulsion Laboratory, California Institute of Technology, 4800 Oak Grove Dr., Pasadena, CA 91109, USA
19. Kavli Institute for Cosmological Physics, University of Chicago, Chicago, IL 60637, USA
20. Instituto de Física Teórica UAM/CSIC, Universidad Autónoma de Madrid, 28049 Madrid, Spain
21. Institut d'Estudis Espacials de Catalunya (IEEC), 08034 Barcelona, Spain
22. Institute of Space Sciences (ICE, CSIC), Campus UAB, Carrer de Can Magrans, s/n, 08193 Barcelona, Spain
23. Center for Astrophysical Surveys, National Center for Supercomputing Applications, 1205 West Clark St., Urbana, IL 61801, USA
24. Department of Astronomy, University of Illinois at Urbana-Champaign, 1002 W. Green Street, Urbana, IL 61801, USA
25. Santa Cruz Institute for Particle Physics, Santa Cruz, CA 95064, USA
26. Center for Cosmology and Astro-Particle Physics, The Ohio State University, Columbus, OH 43210, USA
27. Department of Physics, The Ohio State University, Columbus, OH 43210, USA
28. Center for Astrophysics | Harvard & Smithsonian, 60 Garden Street, Cambridge, MA 02138, USA
29. Australian Astronomical Optics, Macquarie University, North Ryde, NSW 2113, Australia
30. Lowell Observatory, 1400 Mars Hill Rd, Flagstaff, AZ 86001, USA
31. Departamento de Física Matemática, Instituto de Física, Universidade de São Paulo, CP 66318, São Paulo, SP, 05314-970, Brazil
32. George P. and Cynthia Woods Mitchell Institute for Fundamental Physics and Astronomy, and Department of Physics and Astronomy, Texas A&M University, College Station, TX 77843, USA
33. LPSC Grenoble - 53, Avenue des Martyrs 38026 Grenoble, France
34. Institució Catalana de Recerca i Estudis Avançats, E-08010 Barcelona, Spain
35. Department of Astrophysical Sciences, Princeton University, Peyton Hall, Princeton, NJ 08544, USA
36. Observatório Nacional, Rua Gal. José Cristino 77, Rio de Janeiro, RJ - 20921-400, Brazil
37. Department of Physics, Northeastern University, Boston, MA 02115, USA
38. Centro de Investigaciones Energéticas, Medioambientales y Tecnológicas (CIEMAT), Madrid, Spain
39. School of Physics and Astronomy, University of Southampton, Southampton, SO17 1BJ, UK
40. Computer Science and Mathematics Division, Oak Ridge National Laboratory, Oak Ridge, TN 37831
41. Argonne National Laboratory, 9700 S Cass Ave, Lemont, IL 60439, USA
42. Department of Astronomy, University of California, Berkeley, 501 Campbell Hall, Berkeley, CA 94720, USA
43. Lawrence Berkeley National Laboratory, 1 Cyclotron Road, Berkeley, CA 94720, USA